

Field theory Lagrangian approach to nuclear structure

Tapas Sil¹, S. K. Patra², B. K. Sharma², M. Centelles¹, and X. Viñas¹

¹*Departament d'Estructura i Constituents de la Matèria, Facultat de Física,
Universitat de Barcelona, Diagonal 647, 08028 Barcelona, Spain*

²*Institute of Physics, Sachivalaya Marg,
Bhubaneswar 751 005, India.*

Abstract

We show that in the search of a unified mean field description of finite nuclei and of nuclear and neutron matter even at high densities, the relativistic nuclear model derived from effective field theory and density functional theory methods constitutes a competitive framework. The model predicts a soft equation of state, owing to the additional meson interaction terms, consistently with the results of the microscopic Dirac-Brueckner-Hartree-Fock theory and recent experimental observations from heavy ion collisions. In finite systems, after inclusion of the pairing correlations, the model is able to describe both stable and exotic nuclei. We address two examples at the limits of the nuclear landscape. On the one hand, we analyze the giant halo effect and the isoscalar giant monopole resonance in very neutron-rich Zr isotopes. On the other hand, we discuss the structure of superheavy nuclei with double shell closures.

I. INTRODUCTION

The mean field treatment of the relativistic field theory of hadrons known as quantum hadrodynamics (QHD) has been found to be a very successful framework for describing diverse bulk and single-particle properties of nuclear matter and finite nuclei [1, 2, 3]. The QHD theory is based on a Lagrangian density which uses the nucleon (as Dirac particle) and the isoscalar-scalar σ , the isoscalar-vector ω , isovector-vector ρ and the pseudo-scalar π mesons as the relevant degrees of freedom in order to understand many aspects of the nuclear many-body problem. In the relativistic mean field (RMF) approach the nucleus is described in terms of Dirac quasiparticles moving in classical meson fields. Due to the definite ground-state spin and parity of the nuclear system, the contribution of the π meson vanishes at the mean field level. The mean field approximation of QHD automatically generates important ingredients of the nuclear problem like the spin-orbit force, or the finite range and density dependence of the nuclear interaction.

The original linear $\sigma - \omega$ version of QHD [1, 4] gives a very stiff equation of state (EOS) with a nuclear matter incompressibility modulus $K_\infty \sim 600$ MeV. Also, the model does not yield the average properties of the ground-state of finite nuclei in good enough agreement with the experimental values. To remove these deficiencies, the linear $\sigma - \omega$ model was complemented with cubic and quartic non-linearities of the σ meson [5]. Adjusting some coupling constants and meson masses from the properties of a small number of finite nuclei, the non-linear $\sigma - \omega$ model (called hereafter standard RMF model) produces an excellent description of binding energies, radii, spectra, and excitation properties of spherical and deformed nuclei along the whole periodic table [2]. The RMF theory was proposed to be renormalizable, and thus the scalar self-interactions were limited to a quartic polynomial and scalar-vector or vector-vector self-interactions were not allowed. However, the renormalizability of the Lagrangian gets compromised by the use of coupling constants that are not assigned with their bare experimental values but with effective values to have proper results for finite nuclei.

More recently, inspired by the modern concepts of effective field theory (EFT) and of density functional theory (DFT) for hadrons, Furnstahl, Serot and Tang [6, 7] abandoned renormalizability and proposed a chiral effective Lagrangian to derive an energy functional for the nuclear many-body problem. The mean field treatment of the new formulation, now onwards known as E-RMF theory, extends the standard RMF theory by allowing more general couplings [3, 7]. An EFT assumes that there exist natural scales to a given problem and that the only degree of freedom relevant for its description are those which can resolve the dynamics at such scale. The unknown dynamics, which corresponds to heavier degrees of freedom is integrated and appears as coupling constants of the theory, which are fitted to the known experimental data. The Lagrangian of Furnstahl, Serot and Tang has to be understood as an EFT of low-energy QCD. Hence, it contains the lowest-lying hadronic degree of freedom and incorporates all the infinite couplings in general non-renormalizable, consistent with the underlying symmetry of QCD. Therefore, it is mandatory to develop a suitable scheme of expansion and truncation. To do that, one assign first an index ν to each term of the Lagrangian. This index is provided by some organizing principle, as for instance, the naive dimensional analysis [8]. Next the Lagrangian is organized in powers of ν and truncated. For the truncation to be consistent, the coupling constants have to exhibit naturalness (i.e. they are of the order of unity when written in an appropriate dimensionless form) and none of them can be arbitrarily dropped out to given order without any additional symmetry arguments. In the nuclear structure problem, the basic expansion parameters are the ratios of the scalar and vector fields and of the Fermi momentum k_F to the nucleon mass M , as these ratios are small in normal situations (typically $k_F/M = 1/3$ at saturation density).

From the truncated EFT Lagrangian, the energy functional can be constructed in terms of the nuclear densities and auxiliary meson fields. Thus RMF theory can be regarded as a covariant formulation of DFT in the sense of Kohn and Sham [9]. From this energy functional one can define a set of Kohn-Sham equations which minimize the energy with respect to densities and fields. In this way all the source terms in the Kohn-Sham equations are local.

As far as the free parameters of the RMF have been fitted to experimental data, the corresponding mean field energy functional is a good approximation to the exact one, unknown energy functional of the ground state densities of the nucleonic system which includes all higher order correlations, through the powers of the auxiliary classical mean fields. This combination of EFT and DFT provides an approach for dealing with the nuclear problem through Kohn-Sham (Hartree) equations with the advantage that further contributions, at the mean field level or beyond, can be incorporated in a systematic and controlled manner.

References [7, 10, 11] have shown that it suffices to go to fourth order in the expansion parameter ν . At this level one recovers the standard non-linear $\sigma - \omega$ plus some additional non-linear scalar-vector and vector-vector meson interactions besides tensor couplings. The free parameters of the energy functional have been optimized by fitting to the ground-state observables of a few doubly-magic nuclei, as is typical in the RMF strategy. The corresponding fits, that were named G1 and G2 in Ref. [7], display naturalness and the results are not dominated by the last terms retained. This confirms the usefulness of the EFT concepts and validates the truncation of the effective Lagrangian at the first lower orders. The ideas of EFT have allowed [10] to elucidate the empirical success of the previous RMF models, like the original $\sigma - \omega$ model of Walecka [4] and its extensions including cubic and quartic scalar self-interactions [5]. However, these conventional RMF models truncate the Lagrangian at the same level without further physical rationale or symmetry arguments.

The impact of each one of the new couplings introduced in the E-RMF model on the properties of nuclear matter and of the nuclear surface has been analyzed in Ref. [12]. That the model derived from EFT can provide a unified framework to accommodate the successful phenomenology of the traditional RMF models for finite nuclei and to extend them reliably for applications in regions of higher densities than around saturation was shown in Refs. [13, 14]. In fact, nowadays heavy ion collisions can compress nuclear matter in the laboratory to several times the saturation density value. These large densities are

envisaged to be present within core-collapse supernovae and their remnant neutron stars. A common practice in nuclear phenomenology is to extrapolate the models adjusted to the experimental properties of nuclei at normal densities for predictions of such very dense systems. While all the models agree similarly for the normal stable nuclei, their extrapolations can differ significantly. It is therefore meaningful to compare the scenarios for dense matter predicted by the RMF and E-RMF models. Microscopic Dirac-Brueckner-Hartree-Fock calculations [15, 16] and recent experimental data [17, 18] suggest that the nuclear equation of state (EOS) at high densities is rather soft. We will see that the E-RMF energy functional allows one to explain the situation.

During the last decades much effort has been devoted to measure masses of nuclei far from stability. The planned radioactive ion beam facilities bring renewed and well-founded expectations to the field. The available new experimental data turn out to be a demanding benchmark for the predictions of currently existing relativistic and non-relativistic nuclear force parameters. In Ref. [19] we verified the ability of the E-RMF model for describing the ground-state properties of different isotopic and isotonic chains from the valley of β stability up to the drip lines. The residual pairing interaction was treated in a modified BCS approach which takes into account quasibound levels owing to their centrifugal barrier. Also, the convergence of the E-RMF approach was studied for some specific doubly-magic nuclei far from stability in Ref. [20] and remarkable agreement with experiment was found. In the mass region of superheavy nuclei the E-RMF parametrizations have been applied for investigating the next possible shell closures beyond $Z = 82$ and $N = 126$, through the analysis of several indicators such as two-nucleon separation energies, two-nucleon shell gaps, average pairing gaps, and the shell correction energy [21]. Other applications of the model based on EFT include the description of asymmetric nuclear matter at finite temperature [22], calculations of the Landau parameters [23], investigations of the nuclear spin-orbit force [24], or studies of pion-nucleus scattering [25].

The rest of the paper is organized as follows. In the second section we summarize the E-RMF model based on EFT. The third section is devoted to the

study of the infinite nuclear and neutron matter in the E-RMF model, paying special attention to the possible extrapolations to dense systems by comparing with microscopic Dirac-Brueckner-Hartree-Fock calculations [15, 16]. The fourth section exemplifies the ability of the E-RMF model for describing exotic nuclei far from the β -stability line in the case of very neutron-rich Zr isotopes. In the fifth section we analyze the application of the E-RMF model to super-heavy elements. Often, we will compare the predictions obtained from the parametrizations based on EFT with the results from the standard non-linear $\sigma - \omega$ NL3 parameter set [26], taken as a reference. NL3 is regarded as one of the best representatives of the RMF model with only scalar self-interactions because of its proven performance in describing many nuclear phenomena. A summary and the conclusions are given in the last section.

II. FORMALISM

The E-RMF model used here has been developed in Ref. [7], where the reader can find the details of the construction of the effective Lagrangian with a non-linear realization of chiral symmetry. Further insight into the model and the underlying concepts can be gained from Refs. [3, 6, 10, 11]. To solve the equations of motion of the theory one applies the relativistic mean field or Hartree approximation. The meson fields are replaced with their ground-state expectation values, and thus they are treated as classical fields. In such an approach the pseudoscalar field of the pions does not contribute explicitly because it has a vanishing expectation value. The quantum structure is introduced by expanding the nucleon field on a single-particle basis. For systems with time reversal symmetry, as there can be no currents, only the time-like component of the vector meson and photon fields contributes. Charge conservation implies that only the third component in isospin space of the isovector rho-meson field does not vanish. As a final product, one obtains the following energy density functional of the EFT relativistic model for applications to

finite nuclei in mean field approach [3, 7]:

$$\begin{aligned}
\mathcal{E}(\mathbf{r}) = & \sum_{\alpha} \varphi_{\alpha}^{\dagger} \left\{ -i\boldsymbol{\alpha} \cdot \boldsymbol{\nabla} + \beta(M - \Phi) + W + \frac{1}{2}\tau_3 R + \frac{1 + \tau_3}{2} A \right. \\
& - \frac{i}{2M} \beta \boldsymbol{\alpha} \cdot \left(f_v \boldsymbol{\nabla} W + \frac{1}{2} f_{\rho} \tau_3 \boldsymbol{\nabla} R + \lambda \boldsymbol{\nabla} A \right) + \frac{1}{2M^2} (\beta_s + \beta_v \tau_3) \Delta A \Big\} \varphi_{\alpha} \\
& + \left(\frac{1}{2} + \frac{\kappa_3}{3!} \frac{\Phi}{M} + \frac{\kappa_4}{4!} \frac{\Phi^2}{M^2} \right) \frac{m_s^2}{g_s^2} \Phi^2 - \frac{\zeta_0}{4!} \frac{1}{g_v^2} W^4 \\
& + \frac{1}{2g_s^2} \left(1 + \alpha_1 \frac{\Phi}{M} \right) (\boldsymbol{\nabla} \Phi)^2 - \frac{1}{2g_v^2} \left(1 + \alpha_2 \frac{\Phi}{M} \right) (\boldsymbol{\nabla} W)^2 \\
& - \frac{1}{2} \left(1 + \eta_1 \frac{\Phi}{M} + \frac{\eta_2}{2} \frac{\Phi^2}{M^2} \right) \frac{m_v^2}{g_v^2} W^2 - \frac{1}{2g_{\rho}^2} (\boldsymbol{\nabla} R)^2 - \frac{1}{2} \left(1 + \eta_{\rho} \frac{\Phi}{M} \right) \frac{m_{\rho}^2}{g_{\rho}^2} R^2 \\
& - \frac{1}{2e^2} (\boldsymbol{\nabla} A)^2 + \frac{1}{3g_{\gamma}g_v} A \Delta W + \frac{1}{g_{\gamma}g_{\rho}} A \Delta R. \tag{1}
\end{aligned}$$

In the present form the coupling constants should be of order unity according to the naturalness assumption. In Eq. (1) τ_3 is the third component of the isospin operator. The index α runs over all occupied nucleon states $\varphi_{\alpha}(\mathbf{r})$ of the positive energy spectrum. The meson fields are $\Phi \equiv g_s \phi_0(\mathbf{r})$ (isoscalar scalar σ meson), $W \equiv g_v V_0(\mathbf{r})$ (isoscalar vector ω meson), and $R \equiv g_{\rho} b_0(\mathbf{r})$ (isovector vector ρ meson), and the photon field is $A \equiv e A_0(\mathbf{r})$.

From the functional (1) one derives the field equations obeyed by the nucleonic and the mesonic fields. The variation of Eq. (1) with respect to $\varphi_{\alpha}^{\dagger}$ gives the Dirac equation fulfilled by the nucleons, and the variations with respect to the various meson fields result in the Klein-Gordon equations obeyed by the mesons. The expressions for the densities and the field equations of the E-RMF model can be found in previous works [3, 7, 13, 14, 20] and we shall not repeat them here. In practice we solve the Dirac equation in coordinate space by transforming it into a Schrödinger-like equation and iterate numerically the final set of coupled equations till consistency is reached.

Let us now describe the more relevant implications of the new terms of the energy density (1). With the inclusion of the quartic vector self-interaction ζ_0 and the terms η_1 and η_2 one is able to obtain a desirable positive value of the coupling constant κ_4 of the quartic scalar self-interaction. This is so for realistic

nuclear matter properties and at the same time keeping all the parameters within the bounds of naturalness. Furthermore, these bulk couplings ζ_0 , η_1 , and η_2 confer an extra density dependence to the scalar and vector self-energies [13, 14] which is consistent with the output of microscopic Dirac-Brueckner-Hartree-Fock calculations that start from the bare nucleon-nucleon interaction in free space. In the E-RMF model the bulk symmetry energy coefficient J depends on the coupling η_ρ in addition to the usual coupling g_ρ . The new coefficient η_ρ is useful to fit J and in turn to tune, relative to J , the stiffness of the nucleus against pulling neutrons apart from protons as the neutron excess is increased [12].

In the standard RMF model the only parameter not related with the saturation conditions is the mass of the scalar meson m_s . The additional couplings α_1 and α_2 in the E-RMF energy density are helpful to improve on the description of the nuclear surface properties (e.g., surface energy and surface thickness) without spoiling the bulk properties [12]. The quantities β_s , β_v , g_γ and $\lambda = \frac{1}{2}\lambda_p(1 + \tau_3) + \frac{1}{2}\lambda_n(1 - \tau_3)$ take care of effects related with the electromagnetic structure of the pion and the nucleon (the constants $g_\gamma^2/4\pi = 2.0$, $\lambda_p = 1.793$ and $\lambda_n = -1.913$ are given their experimental values) [7]. The tensor coupling f_v between the ω meson and the nucleon adds momentum and spin dependence to the interaction. It introduces a corrective term in the spin-orbit potential as compared with the expression in the standard RMF model [19, 24]. Due to the existence of a trade-off between the size of the ω tensor coupling and the size of the scalar field, it is possible to obtain parameter sets that provide excellent fits to nuclear masses, radii and spin-orbit splittings with a larger value of the equilibrium effective mass than in models that ignore such coupling.

In the applications to be presented below we shall employ the E-RMF parameter sets G1 and G2 of Ref. [7]. The masses of the nucleon and of the ω and ρ mesons are $M = 939$ MeV, $m_v = 782$ MeV, and $m_\rho = 770$ MeV, respectively. The parameters m_s , g_s , g_v , g_ρ , η_1 , η_2 , η_ρ , κ_3 , κ_4 , ζ_0 , f_v , α_1 , and α_2 of G1 and G2 were fitted by a least-squares optimization procedure to 29 observables (binding energies, charge form factors and spin-orbit splittings near

the Fermi surface) of the nuclei ^{16}O , ^{40}Ca , ^{48}Ca , ^{88}Sr and ^{208}Pb , as described in Ref. [7]. The constants β_s , β_v and f_ρ were then chosen to reproduce the experimental charge radii of the nucleon. We report in Table 1 the values of the parameters and the saturation properties of the sets G1 and G2 as well as those of the NL3 parameters [26]. An interesting feature is that the set G2 has a positive κ_4 coupling, as opposed to G1 and to most of the successful RMF parametrizations such as NL3. Formally, a negative value of κ_4 is not acceptable because the energy spectrum then has no lower bound [27]. We note that the value of the effective mass at saturation M_∞^*/M in the EFT sets (~ 0.65) is larger than the usual value in the RMF parameter sets (~ 0.60), which is due to the presence of the tensor coupling f_v of the ω meson to the nucleon. Also, the nuclear matter incompressibility of the G1 and G2 sets ($K = 215$ MeV) is visibly smaller than that of the NL3 set ($K = 271$ MeV).

III. NUCLEAR AND NEUTRON MATTER

In an infinite medium of uniform nuclear matter all of the terms with gradients in the energy density \mathcal{E} and in the field equations vanish. In this limit the nucleon density is given by

$$\rho = \frac{\gamma}{(2\pi)^3} \int_0^{k_F} d^3k = \frac{\gamma}{6\pi^2} k_F^3, \quad (2)$$

where k_F is the Fermi momentum, and the degeneracy factor γ is 4 for symmetric nuclear matter and 2 for pure neutron matter. The reader can find the E-RMF expression of \mathcal{E} for asymmetric nuclear matter at finite temperature in Ref. [22].

The relevance of relativistic effects in the nuclear EOS was soon realized when the relativistic Dirac-Brueckner-Hartree-Fock (DBHF) calculations provided a clue for solving the Coester band problem [15]. The microscopic DBHF theory suggests a soft EOS at high densities [15, 28]. The recent experimental data [17, 18] also rule out the possibility of a strongly repulsive nuclear EOS. Typical representatives of the standard RMF theory like the NL3 parameter set cannot follow the trend of the DBHF results even at slightly high densities

[13]. In contrast to the conventional RMF model, the E-RMF calculations at high density regimes yield results in accordance with the DBHF theory. It has to be noted that relativistic models which resort to density-dependent couplings are also consistent with the DBHF calculations [29].

In Figure 1 we present the density dependence of the nuclear matter scalar and vector self-energies calculated with G1, G2, NL1 [30] and NL3 versus the DBHF result. While G2 follows the nature of the DBHF self-energies quite remarkably, at densities only slightly above saturation the NL3 results soon depart from the DBHF behaviour. Thus, the success of the usual RMF model with only scalar self-interactions for describing the saturation point and the data for finite nuclei is not followed by a proper description of the microscopic DBHF calculations. This is caused importantly by a too restrictive treatment of the ω -meson term [13, 14, 28]. While in the standard RMF model the vector potential increases linearly with density and gets stronger, in DBHF it bends down with density. Moreover, the scalar potential overestimates the DBHF result at high density in order to compensate for the strong repulsion in the vector channel. The additional self- and cross-interactions ζ_0 , η_1 , and η_2 included in the E-RMF sets result in a richer density dependence of the mesonic mean fields which brings about the improvement in comparison with the DBHF calculations [13].

Figure 1 demonstrates the importance of meson self-interactions at higher densities and exposes the inadequacy of restricted models which neglect them for applications to such conditions. This argument is further supported by Figure 2 in which the variation of the binding energy per particle is plotted as a function of the density. We can see that the calculations of dense matter based on the RMF sets NL1 and NL3 deviate largely from DBHF, while the E-RMF calculations with G1 and, specially, G2 agree better with the density dependence of the EOS of the DBHF theory. One can realize that in spite of the fact that the incompressibility of NL1 is within the empirical boundaries ($K_\infty = 212$ MeV for NL1), the EOS of this set soon becomes stiff with increasing density and does not follow the DBHF trend. The E-RMF parameter sets give a soft EOS both around saturation and at high densities. A sim-

ilar situation prevails in the EOS of neutron matter (Figure 3), though the agreement of G1 and G2 with the DBHF calculation is not as remarkable as in the case of symmetric matter. From the point of view of the comparison with DBHF, this would indicate that the present E-RMF model still needs an improvement in the treatment of the isovector sector, like consideration of additional cross couplings involving the rho-meson field or the introduction of an isovector scalar meson.

The average densities of terrestrial nuclei are not very far from the values around the saturation point of the nuclear EOS, where the E-RMF sets produce similar results to NL3. Hence, one can expect that in finite nuclei the G1 and G2 interactions also will yield results on a par with the celebrated NL3 parametrization. That this is indeed the case is illustrated in the next section for the bulk properties of finite nuclei near and away from the β -stability valley.

IV. STRUCTURE OF EXOTIC NUCLEI

Exotic nuclei far from the stability line have attracted much attention in the nuclear physics community from both the theoretical and the experimental sides. One expects to find very different properties from the normal nuclei as soon as one leaves the β -stability region and approaches the drip lines. Neutron-rich nuclei near the drip line and the occurrence of closed shells are very important in nuclear astrophysics because their properties strongly influence how stable neutron-rich nuclei are formed through the r-process. It is expected that in very neutron-rich nuclei the shell structure be strongly modified, with some of the traditional shell gaps disappearing and with new ones appearing.

Another interesting feature of some exotic nuclei is the appearance of a halo structure which was experimentally discovered in ^{11}Li [31] and which has also been observed in $^{11,14}\text{Be}$ and ^{17}B [32]. In some heavier neutron rich nuclei a sudden increase of the neutron radii close to the neutron drip line, the so-called giant halo, has been predicted by theoretical relativistic Hartree-Bogoliubov (RHB) calculations for Zr [33] and Ca [34] isotopes.

Neutron-rich nuclei near the drip line usually have a very small Fermi level and thus valence nucleons can easily scatter to the continuum states through the pairing correlations. Consequently, it is mandatory to properly take into account the coupling between the bound and the continuum for dealing with nuclei near the drip lines. In the relativistic domain, the microscopic HFB theory should, in principle, be used. Although the simple BCS theory fails in describing nuclei near the drip lines [35], it can still be used if some refinements to the standard BCS method are added, such as the resonant continuum coupling [36, 37] or if one takes into account quasibound levels owing to their centrifugal barrier [13]. These variations of the BCS method in general allow one to describe nuclei in the vicinity of the drip lines with very reasonable accuracy and avoiding the difficulties of a full RHB calculation.

In this section, we analyze the giant halo effect in Zr isotopes using the E-RMF approximation together with the pairing prescription of Ref. [13] which allows one to describe isotopic (isotonic) chains with magic Z (N) numbers from the proton to the neutron drip lines. As far as many properties of the exotic nuclei are modified when one approaches the drip line, we will discuss afterwards a different problem related with excited states, namely, the excitation energy of the isoscalar giant monopole resonance. From nonrelativistic RPA calculations [38] it is known that in nuclei near the drip line the monopole strength distribution is much affected by the presence of the low-energy threshold stemming from tiny bound nucleons. We study here whether the E-RMF parametrizations in constrained calculations are able to identify the main trends exhibited by the monopole RPA strength near the drip lines.

A. Treatment of pairing

To deal with the pairing correlations we shall use here a simplified prescription which has proven to be in good agreement with RHB calculations [19]. For each kind of nucleon we assume a constant pairing matrix element G_q , which simulates the zero range of the pairing force, and include quasibound levels in the BCS calculation as done in Ref. [39]. These quasibound states

mock up the influence of the continuum in the pairing calculation. We restrict the available space of α_q states to one harmonic oscillator shell above and below of the Fermi level, to avoid the unrealistic pairing of highly excited states and to confine the region of influence of the pairing potential to the vicinity of the Fermi level. As explained in Ref. [13], the solution of the pairing equations provides the chemical potential μ_q and the average pairing gap Δ_q for each kind of nucleon.

The quasibound levels of positive single-particle energy are retained by the centrifugal barrier (neutrons) or the centrifugal-plus-Coulomb barrier (protons). The wave functions of the considered quasibound levels are mainly localized in the classically allowed region and decrease exponentially outside it. As a consequence, the unphysical nucleon gas which surrounds the nucleus if continuum levels are included in the normal BCS approach is eliminated. We have shown in Ref. [19], by comparison with available RHB results, that the procedure is able to predict well the position of the proton and neutron drip lines or, e.g., the behavior of the neutron and charge radii far from stability. Also, the calculated pairing gaps turn out to be scattered around the empirical average $12/\sqrt{A}$ MeV.

B. Giant halo in Zr isotopes

As we have mentioned, giant halo nuclei are predicted by the RMF calculations near the neutron drip line for Zr [33] and Ca [34] isotopes. With the new radioactive isotope beam facilities it is expected to reach experimentally the lighter giant halo nuclei of Zr. Our calculation is performed with the E-RMF set G2 in spherical symmetry due to the fact that non-relativistic and relativistic calculations above ^{122}Zr predict the nuclei to be spherical [33]. The neutron and proton constant matrix elements are parametrized as $G_q = C_q/A$ ($q = p, n$). In the calculations presented in this section we choose $C_n = 16$ MeV and $C_p = 14$ MeV because with these pairing constants we obtain pairing correlation energies (i.e., binding energies referred to the E-RMF values without pairing) from ^{122}Zr to ^{138}Zr similar to those displayed in Figure 5 of Ref.

[37]. The latter calculation was performed in the BCS-plus-resonant (r-BCS) continuum approximation with the RMF parameter set NL-SH employing a zero-range pairing force, which simulated well the RHB calculations of Ref. [33] with NL-SH.

One of the signatures of the giant halo consists in a sudden increase of the neutron root mean square (rms) radius in the isotopic chain due to the scattering of Cooper pairs to the continuum containing low-lying resonances of small angular momentum, which in our approach are represented by the quasibound levels. Figure 4 displays the neutron and proton rms radii for the Zr isotopic chain from $A = 80$ to $A = 120$ obtained using our pairing approach with the G2 parameter set. One can clearly appreciate the kink at $A = 122$. The neutron radii obtained with G2 reproduce the overall trends of the results of Ref. [37] that were computed with the NL-SH set in the r-BCS approximation. It is to be noted that we use a pairing force with a constant matrix element instead of a zero-range pairing force as in Ref. [37]. Another difference with Ref. [37] is that our calculation does not take into account the resonance width, which may contribute to reduce the pairing gap near the drip line.

The Zr isotopes with a neutron number beyond $N = 82$ develop a large shell gap and start progressively to fill up the weakly bound and quasibound (continuum) $2f_{7/2}$, $3p_{3/2}$, $3p_{1/2}$, $2f_{5/2}$, $1h_{9/2}$ and $1i_{13/2}$ single-particle neutron energy levels. This can be seen in Figure 5 where the neutron spectra of two representative nuclei, ^{128}Zr and ^{140}Zr , are displayed. In our model the $1i_{13/2}$ and $1h_{9/2}$ are quasibound levels and correspond to low-lying resonant levels [37]. The $3p_{1/2}$ and $2f_{5/2}$ levels lie in the continuum up to $A = 134$ and $A = 140$, respectively, while the $2f_{7/2}$ and $3p_{3/2}$ states are always bound levels from $A = 124$ on. It should be pointed out that the considered levels lying in the continuum are always quasibound levels for $N = 82$ owing to their relatively high centrifugal barrier ($l > 2$). In our calculation only the $3p_{1/2}$ orbit does not appear as a quasibound level because of its small centrifugal barrier.

It is just the occupancies of $2f_{7/2}$, $3p_{3/2}$, $3p_{1/2}$, and $2f_{5/2}$ levels which mainly

contribute to the enhancement of the neutron rms beyond $N = 82$, as discussed in earlier literature [33, 37]. In the lighter Zr isotopes one observes the progressive filling of the $1h_{11/2}$ state and the almost negligible occupancy of the states beyond the $N = 82$ core. After $N = 82$, the occupancy of the weakly bound and quasibound $3p_{3/2}$, $3p_{1/2}$, $2f_{5/2}$, $1h_{9/2}$ and $1i_{13/2}$ states starts to be progressively important when the number of neutrons beyond the core increases. In our model, the $3p_{1/2}$ state appears when $A = 134$ as a tiny bound state which causes the small kink between $A = 132$ and $A = 134$ that can be seen in Figure 4.

The rms radii of the neutron orbits above the $N = 82$ core and of the $2d_{3/2}$ and $1h_{11/2}$ states of the core, as well as the radii of the quasibound $1h_{9/2}$ and $1i_{13/2}$ levels, are displayed in Figure 6. The large rms radii of the $2f_{5/2}$, $3p_{3/2}$ and $3p_{1/2}$ orbits can clearly be seen in this figure. These large rms radii are basically due to two different reasons. First, the principal quantum number n is large (2 or 3) which makes the wave functions corresponding to these orbitals extend quite far. The second reason lies in the fact that the $2f_{5/2}$, $3p_{3/2}$ and $3p_{1/2}$ levels are extremely weakly bound, or even unbound, for $N > 82$. For instance, the single particle energy of the $3p_{3/2}$ level runs from -0.16 MeV in ^{124}Zr to -0.77 MeV in ^{140}Zr . Due to the last reason, these levels show up a relatively strong dependence with the mass number A . However, the rms radii of the $1h_{11/2}$ and $2f_{7/2}$ orbitals are roughly constant with A due to the larger binding energy of these states. The quasibound $1h_{9/2}$ and $1i_{13/2}$ states also exhibit a nearly constant rms radii as a function of A . In this case the reason is rather that the small principal quantum number ($n = 1$) pushes the significant part of the wave function inside enough for not being affected by the increasing number of nucleons outside the ^{122}Zr core. We note that for obtaining the contribution of the states displayed in Figure 6 to the total neutron rms radius, the degeneracy $2j + 1$ and the occupancy v^2 of these levels has to be taken into account, which gives an increasing contribution with A . For instance, the contribution to the total $\langle r_n^2 \rangle$ radius from the $2f_{7/2}$, $3p_{3/2}$ and $2f_{5/2}$ states is 0.59, 0.50 and 0.06 fm² in ^{124}Zr , whereas it is 2.63, 1.80 and 1.53 fm² in the drip line nucleus ^{140}Zr . This explains the increasing tendency

of the rms radii in Figure 4 beyond the $N = 82$ core.

Another indicator of a giant halo is a very small neutron chemical potential μ_n . This is just the situation we find using the E-RMF set G2, with the discussed pairing prescription, in the neutron rich Zr isotopes beyond $N = 82$. In our calculation, μ_n ranges from -0.89 MeV for ^{124}Zr to practically zero in ^{140}Zr . As a consequence of this almost vanishing value of μ_n beyond the $N = 82$ core, the binding energies are roughly constant, ranging from 943.7 MeV in ^{124}Zr to 951.9 MeV in ^{140}Zr , and the two-neutron separation energies S_{2n} are close to zero. We have calculated the two-neutron separation energies along the Zr isotopic chain for the G2 and NL-SH parameter sets. In both parameter sets shell effects appear at $N = 50$ and 82 , as expected. Beyond $N = 82$, S_{2n} decreases faster for NL-SH than for G2 indicating that although the general features of giant halo nuclei are unchanged, fine details can be force dependent. In Figure 7 we display the calculated neutron densities of some selected Zr isotopes. When the neutron number is significantly above the $N = 82$ core the central density starts to progressively decrease, while a halo develops in the outer region. Some neutrons of the core are scattered by the pairing correlations to the states beyond the Fermi level, with larger rms radii with the increasing number of the neutrons in the outer part of the density distribution of the nuclei beyond ^{122}Zr .

The simplified treatment of the pairing correlations used here, which is discussed in more detail in Ref. [19], is thus seen to be able to describe the bulk properties of nuclei near the drip lines [13, 19] and also to reproduce correctly the main features of the giant halo nuclei. Only some finer details such as the behavior of the $3p$ levels in the giant halo problem discussed here, would require of an improved treatment of the pairing correlations using more sophisticated methods such as the r-BCS or RHB approaches. On the other hand, the study presented here, together with the examples discussed in Refs. [13, 19], proves the ability of the RMF approach based on EFT for describing exotic isospin-rich nuclei far from the β -stability valley when a pairing residual interaction is included. Notice that only information about a few stable magic nuclei was used in the fit of the coupling constants of the E-RMF sets, and

thus the results near the drip lines are predictions of the model.

C. Breathing mode energy near the neutron drip line

It is to be expected that in neutron rich nuclei, and in particular in giant halo nuclei, the excitation energy of collective modes be strongly modified as compared with stable nuclei. For further prospect, we next address with the example of the Zr isotopes the trends predicted by the G2 set for the behavior of the excitation energy of the isoscalar giant monopole resonance (GMR) in approaching the limits of neutron stability. As we have seen in the previous subsection, in Zr isotopes beyond $A = 122$ the last filled levels are weakly bound. Thus, particle-hole excitations from the occupied $2f_{7/2}$, $3p_{3/2}$, $3p_{1/2}$ and $2f_{5/2}$ states to the continuum will give important contributions to the low-energy part of the RPA strength. The situation for these Zr isotopes is similar to that found in the ^{110}Ni nucleus for which the RPA strength has been analyzed in Ref. [38] by means of non-relativistic Skyrme force calculations. Although in such kind of very neutron-rich nuclei the monopole RPA strength is broad and it is not concentrated in a single peak [38], the mean energy of the monopole response should exhibit a downwards behavior when one moves from stable nuclei towards the neutron drip line due to the increase of the amount of strength in the low energy region of the resonance.

Constrained calculations are one of the means to estimate the average energy of the breathing mode. For example, RMF constrained calculations have been performed with different parameter sets to obtain the excitation energies of the GMR of some selected nuclei in Refs. [40, 41, 42, 43]. A reasonable good agreement has been found between the results of these calculations with the results from more sophisticated approaches such as the time-dependent RMF formalism [44] or the relativistic RPA [45].

Here we follow the method of Refs. [40, 41, 42, 43] to perform the constrained calculations with the E-RMF model. One has to solve the self-consistent equations for the nucleonic and mesonic fields derived from the

constrained energy

$$E_c(\eta) = \int d\mathbf{r} \left[\mathcal{E} - \eta \sum_{\alpha} \varphi_{\alpha}^{\dagger} (r^2 - R_0^2) \varphi_{\alpha} \right], \quad (3)$$

where \mathcal{E} is the energy density given by Eq. (1) and R_0 the rms radius of the ground state. The solution of the corresponding equations of motion gives spinors $\varphi_{\alpha}(\eta)$ and mesonic fields which depend on the Lagrange multiplier η .

The binding energy $E(\eta)$, obtained by integrating Eq. (1) with the nuclear and meson fields solution to the constrained problem, has a minimum at $\eta = 0$ which corresponds to the ground-state energy with rms radius R_0 . Expanding $E(\eta)$ in a harmonic approximation about R_0 one obtains the constrained incompressibility of the finite nucleus as

$$K_A^c = \frac{1}{A} R_0^2 \left. \frac{\partial^2 E(\eta)}{\partial R_{\eta}^2} \right|_{\eta=0}, \quad (4)$$

with R_{η} being the rms radius computed with the constrained spinors $\varphi_{\alpha}(\eta)$. The constrained incompressibility of Eq. (4) is just the constant entering the harmonic restoring force.

The mass parameter of the monopole oscillation is given by

$$B = \frac{1}{A} \int d\mathbf{r} u(\mathbf{r})^2 \mathcal{E}(\mathbf{r}), \quad (5)$$

where $u(\mathbf{r})$ is the displacement field which is determined by the solution of the continuity equation for the monopole oscillation [40, 41, 42, 43]. In the non-relativistic limit and with a Tassie transition density, which assumes that there exists a single-collective state, the displacement field is $u(r) = r$ and the expression of the mass parameter becomes

$$B_{nr} = M \int d\mathbf{r} r^2 \rho(\mathbf{r}) = M \langle r^2 \rangle. \quad (6)$$

The frequency of the constrained monopole vibration using the non-relativistic mass parameter is

$$E_c = \sqrt{\frac{A K_A^c}{B_{nr}}}. \quad (7)$$

We have performed the constrained calculation switching off the pairing correlations, as in the non-relativistic studies of giant resonances in nuclei near

the drip lines [38]. Our estimate of the excitation energy of the GMR of the nucleus ^{90}Zr from the constrained calculation with the E-RMF set G2 is 17.2 MeV. It agrees fairly well with the experimental centroid energy 17.9 ± 0.2 MeV [46].

Figure 8 displays the finite nucleus incompressibility K_A^c calculated using the G2 set for even Zr isotopes ranging from $A = 90$ to $A = 138$. The finite nucleus incompressibilities are roughly constant from $A = 90$ up to $A = 122$, when the $1h_{11/2}$ level is completely filled. From $A = 122$ on, the finite nucleus incompressibility decreases quite fast till the neutron drip line is reached. One can try to understand qualitatively this downward tendency as follows. Inspired by the liquid drop formula, the finite nucleus incompressibility can be expanded [47] into a bulk contribution K_∞ (the nuclear matter incompressibility modulus), plus surface K_{surf} , Coulomb K_{Coul} and volume-symmetry K_{sym} terms, apart from corrections of higher order. Within a scaling model approach the quantities K_{surf} , K_{Coul} , and K_{sym} are negative [43, 49]. When the mass number A increases approaching the drip lines, the surface and Coulomb terms become comparatively less important. However, the symmetry contribution, which is large in the RMF parametrizations, multiplied by a large average asymmetry factor $(N - Z)^2/A^2$ makes finally the nuclei near the neutron drip line softer than the stable nuclei. Though the numerical coefficients of the expansion of the nucleus incompressibility K_A into its various contributions are different between the scaling and the constrained models [47, 48], one can still expect that the volume-symmetry term is at the origin of the reduction of K_A^c as the nuclei come close to the neutron drip point.

From a more microscopic point of view, when $A > 122$ the weakly bound neutron levels $2f_{7/2}$, $3p_{3/2}$, $3p_{1/2}$ and $2f_{5/2}$, which have a large rms radius (see Figure 6), start to be occupied. Neutrons in these levels behave almost as extremely asymmetric nuclear matter, which is strongly softened as compared with the symmetric one [50]. According to this, when the number of neutrons outside the $A = 122$ core increases, their contribution to K_A^c is smaller and thus, on average, the finite nucleus incompressibility of the Zr isotopes that develop a giant halo is smaller than the one of the stable Zr nuclei.

Due to the fact that the Zr nuclei beyond $A = 122$ have a large rms radius, the mass denominator (6) also increases when one moves from $A = 122$ towards the neutron drip line. This fact together with the decreasing of the finite nucleus incompressibility reduces strongly the excitation energy of the GMR beyond $A = 122$, as evidenced by Figure 8. It is known that the experimental GMR excitation energies roughly follow the empirical law $E_{\text{GMR}} \sim 80A^{1/3}$ MeV [47]. The excitation energy of the GMR of the Zr isotopes from $A = 90$ to $A = 122$ can be nicely fitted by an $A^{1/3}$ law, as indicated by the dashed line in Figure 8. This behaviour breaks down for the isotopes with $A > 122$ pointing out again that for these nuclei the neutrons which occupy the weakly bound levels above the $1h_{11/2}$ orbit are softer than the neutrons belonging to the $A = 122$ core.

As shown in Ref. [43], the energy of the constrained monopole oscillation (7) can be nominally written in the nonrelativistic language of RPA sum rules as $E_c = \sqrt{m_1/m_{-1}}$ [51]. The sum rules, or moments of the strength function $S(E)$ of the giant resonance, are defined as

$$m_k = \int_0^\infty E^k S(E) dE \quad (8)$$

for integer k . The m_1 sum rule turns out to be proportional to the mass denominator B_{nr} , while the inverse energy weighted sum rule m_{-1} can be computed as [51]

$$m_{-1} = -\frac{1}{2}A \frac{\partial R_\eta^2}{\partial \eta} \Big|_{\eta=0} = \frac{1}{2} \frac{\partial^2 E(\eta)}{\partial \eta^2} \Big|_{\eta=0}. \quad (9)$$

From this point of view, the strong reduction of E_c when $A > 122$ is basically due to an increasingly large inverse energy weighted moment of the RPA strength. The latter, due to the power E^{-1} in (8), reflects the important contribution to the low-energy part of the RPA strength distribution which arises from the particle-hole transitions to the continuum from the weakly bound energy levels $2f_{7/2}$, $3p_{3/2}$, $3p_{1/2}$ and $2f_{5/2}$.

V. PREDICTIONS IN THE LAND OF SUPERHEAVY ELEMENTS

In continuance of our study of the nuclear structure predictions of the E-RMF model in the regions of the nuclear landscape away from the stable nuclei where the parameters were fitted, in this section we address spherical calculations of superheavy elements (SHE). We shall concentrate on finding out where the next doubly-magic shell closures beyond $N = 126$ and $Z = 82$ are located according to the E-RMF model.

Experimental efforts at the leading laboratories for synthesizing new elements in the superheavy mass region have already produced some light isotopes of $Z = 110$ – 112 at GSI and Dubna [52] and even heavier isotopes of $Z = 112$ – 116 at Dubna [53]. Most of the detected nuclei with $Z \sim 110$ are deformed, consistently with the predicted occurrence of a deformed shell closure at $Z = 108$ and $N = 162$ [54, 55, 56]. Therefore, quadrupole deformations [54, 55, 56, 57, 58], and even in some cases triaxial calculations [59], have to be taken into account for describing the new nuclei around $Z = 110$. However, when one is concerned with identifying the location of the N and Z values of the next spherical *double* shell closure beyond ^{208}Pb , most of the calculations with relativistic and non-relativistic mean field models have been performed in spherical symmetry [60, 61, 62, 63]. Of course, one has to keep in mind that the study of the spherical shell structure is valid only for the doubly-magic nuclei. The addition of deformation degrees of freedom in the calculations would certainly change the picture in the details and add deformed shell closures, e.g., like those predicted around $Z = 108$ and $N = 162$ [54, 55, 56]. But it should not change drastically the predictions for the values of N and Z where the strongest shell effects show up already in the spherical calculation. Certainly, for a quantitative discussion, one needs to account for deformation effects which would serve to extend the island of shell stabilized superheavy nuclei and to decide on the specific form of the ground-state shapes of those nuclei.

In the nonrelativistic framework, the macroscopic-microscopic models predict spherical shell closures at $Z = 114$ and $N = 184$ [55]. The Hartree-Fock

calculations with Skyrme forces show, in general, the most pronounced shell effects at $Z = 124$, $Z = 126$ and $N = 184$ [60, 61, 62, 63]. However, the conventional RMF theory typically prefers $Z = 120$ and $N = 172$ as the best candidates for spherical shell closures [60, 61, 62, 63]. In view of these discrepancies in the predicted shell closures for SHE, it is interesting to reinvestigate them using the more general E-RMF model.

A. Shell closures

In normal nuclei a large gap in the single-particle spectrum is interpreted as the indication of a shell closure. We start by inspecting the neutron single-particle spectra of the $^{292}120$, $^{304}120$ and $^{378}120$ nuclei, displayed in Figure 9, calculated using the G1, G2 and NL3 parameter sets. As mentioned, $Z = 120$ is found to be a magic number in many RMF calculations [60, 61, 62, 63]. The three parameter sets show a large gap at $N = 172$ and $N = 258$. However, for $N = 184$ a moderate gap is found mainly for the E-RMF sets, G1 and G2, which is smaller for NL3. In the level spectrum of the system with $N = 258$ and $Z = 120$, one can again find appreciable energy gaps across the neutron numbers $N = 198$ ($1j_{13/2}$ level) and $N = 228$ ($1k_{17/2}$ level) in all the considered parameter sets. By comparing the spectra for the three systems with $N = 172$, 184 and 258, it can be noticed that the gap between two particular levels is strongly modified along the isotopic chain. However, the level gaps are not as distinct as in lighter nuclei. In calculations of SHE the level spectra become very involved due to the presence of levels with a high degree of degeneracy. Therefore, it is imperative to look for other quantities to be able to reliably identify the shell closures and magic numbers of SHE, apart from the analysis of the single-particle level structure.

We next shall consider three energy indicators for locating the nucleon shell closures. First, a sudden jump in the two-neutron (two-proton) separation energies of even-even nuclei, defined as $S_{2q} = E(N_q - 2) - E(N_q)$, where N_q is the number of neutrons (protons) in the nucleus for $q = n$ ($q = p$). Second, the two-neutron (two-proton) shell gap defined as the second difference of the

binding energy [60]: $\delta_{2q}(N_q) = E(N_q + 2) - 2E(N_q) + E(N_q - 2)$. This quantity measures the size of the step found in the two-nucleon separation energy and, therefore, it is strongly peaked at magic shell closures. Third, for closed shell nuclei the average pairing gaps Δ_q obtained in the calculations should vanish.

In Figure 10, we display these energy indicators calculated with the E-RMF set G2 and with NL3 along the isotopic chain of $Z = 120$. The two-neutron separation energies S_{2n} , displayed in the top panel of the figure, show sudden jumps after the neutron numbers $N = 172$, 184 and 258 indicating possible neutron shell closures. The two-neutron shell gap δ_{2n} along the same isotopic chain is displayed in the middle panel of Figure 10. Sharp peaks in δ_{2n} are found at the same neutron numbers 172, 184 and 258, though the peak at $N = 184$ is less pronounced than the peaks for $N = 172$ and $N = 258$. Also, the peak in δ_{2n} at $N = 258$ is more marked in NL3 than in G2. The curve for the neutron pairing gaps displayed in the bottom panel of Figure 10 shows a structure of arches which vanish only at $N = 172$, 184 and 258 with G2, and at $N = 172$ and 258 with NL3. Therefore, all the three analyzed observables point out to the same neutron numbers as the best candidates for shell closures for $Z = 120$ with the G2 parametrization. The neutron pairing gap calculated with NL3 does not vanish at $N = 184$. The proton pairing gap is zero along the whole isotopic chain, for both G2 and NL3, and thus we have not plotted it. The results obtained with the set G1 show the same global nature as with G2 and NL3. The peak in δ_{2n} occurring at $N = 172$ is lower in G1 than in G2, and the peak at $N = 184$ is very much quenched in the G1 set. As in the case of NL3, the neutron gap Δ_n at $N = 184$ does not vanish for G1 ($\Delta_n \approx 0.7$ MeV).

Now we proceed to the discussion of the isotonic chains of $N = 172$ and $N = 184$ obtained with E-RMF set G2 and which are displayed in Figure 11. For $N = 172$ all the indicators show a very robust closure at $Z = 120$ and a much weaker shell closure at $Z = 114$. This is appreciated, e.g., from the strength of the corresponding two-proton shell gap δ_{2p} . For $N = 184$ proton shell closures are found at $Z = 114$ and $Z = 120$. In this case the strength of δ_{2p} for both atomic numbers is similar (though smaller than the two-proton

shell gap found with the combination $N = 172$ and $Z = 120$). Moreover, from the left bottom panel of the Figure 11, it can be seen that below $Z = 110$, the neutron pairing gap does not vanish, meaning that the shell closure for $N = 172$, which is very strong combined with $Z = 120$, is washed out. Thus, in SHE the magicity of a particular neutron (proton) number very much depends on the number of protons (neutrons) present in the nucleus.

From the above discussions we conclude that the E-RMF parameter set G2 clearly points out towards the robust double magic character of the combinations $(N = 172, Z = 120)$ and $(N = 258, Z = 120)$. Similar conclusions are obtained with the G1 and NL3 parameter sets [21]. Also, for the particular case of the new set G2 the combinations $Z = 114$ and $Z = 120$ with $N = 184$ show evidences of a shell closure, although less strong than in the previous cases. A double shell closure in the $(Z = 114, N = 184)$ nucleus has been traditionally predicted by the macroscopic-microscopic models [55].

B. Shell corrections

The indicators discussed in the previous section, which allow one to identify the doubly magic nuclei, correspond to energy differences between neighbouring nuclei. However, they do not have a direct connection with the shell corrections which stabilize a given SHE against fission. In a liquid droplet model picture SHE are unstable against spontaneous fission due to the fact that the large Coulomb repulsion cannot be compensated by the nuclear surface tension. However, SHE may still exist because the quantal shell corrections generate local minima in the nuclear potential energy surface which provide additional stabilization. For experimentally known shell closures (up to $N = 126$ and $Z = 82$), the shell corrections are strongly peaked around the magic numbers [64]. Thus, the shell correction energy also represents a test for checking the robustness of the shell closures.

In Figure 12 we display the total (neutron-plus-proton) shell correction energies calculated employing the Strutinsky smoothing procedure [21, 65] for the $Z = 114$ and $Z = 120$ isotopic chains, using the parameter sets G2 and

NL3. The calculations have been performed in spherical symmetry and thus the computed shell corrections represent in general an upper bound to the actual ones. Deformation could bring additional shell stabilization. From the figure one can see that the isotopic chain of $Z = 120$ shows a large negative shell correction for $N = 172$. Another local minimum, less pronounced, is also found around $N = 182 - 184$. One observes that in superheavy nuclei the shell correction energy at the shell closures does not display the very sharp jumps typical of normal mass nuclei. Rather, the shell corrections depict a landscape of broad areas of shell stabilized nuclei [61, 62, 63]. Still, in these areas the closed shell superheavy nuclei show more negative shell corrections than their neighbours. Looking at the results for $Z = 114$ presented in Figure 12 it can be realized that the shell corrections in the $Z = 114$ isotopes are weaker than for the $Z = 120$ chain, which means less stability. Again, two dips are found at $N = 172$ and $N = 184$, although in this case the minimum at $N = 184$ is deeper than the one at $N = 172$. The study of the shell correction energy reveals that the shell stabilized regions of SHE are in good agreement with the previous predictions for shell closures derived from the analysis of the energy indicators.

C. Density profiles and spin-orbit potentials

From a naive point of view one expects that for a large nucleus the neutron density profile will show a relatively flat region at the interior, modulated by some wiggles due to shell effects. In the case of protons one also expects that the Coulomb repulsion will push them towards the surface so that the proton density will develop a depression in the center. However, some deviations from this pattern can arise in superheavy nuclei. To exemplify the situation, we display in Figure 13 the density profiles of neutrons and protons for the superheavy nuclides $^{292}120$ (close to the proton drip point), $^{304}120$, and $^{378}120$ (close to the neutron drip point). For the purpose of comparison with the situation in smaller nuclei, we have drawn in the same figure the neutron and proton density profiles of the isotopes ^{100}Sn (proton drip line nucleus), ^{132}Sn ,

and ^{176}Sn (neutron drip line nucleus).

Inspecting the behavior of the tin isotopes with increasing neutron number N , one observes that the neutron density extends progressively toward the outside, while it shows only a small increase in the interior. Driven by the proton-neutron interaction, the proton density also extends more and more to the outside. As a result, since $Z = 50$ is fixed, there is a notable reduction of the average proton density in the nuclear interior. (See Ref. [66] for a detailed RHB study of the tin chain.) These general trends are also observed in the evolution with N of the nucleon densities of the $Z = 120$ isotopes displayed on the left side of Figure 13.

It is immediately noted that the neutron density profile of the $^{292}120$ super-heavy nucleus shows an accentuated dip from $r \sim 4$ fm to the origin. As also pointed out in Ref. [60], the reason lies in the fact that for $N = 172$ the last filled neutron levels correspond to a large orbital angular momentum (2g and 1j levels, see Figure 9). Such orbits are mainly located at the surface and thus generate the central dip. This is not the case for the system with $N = 184$, where the last occupied neutron levels (4s and 3d) give an important contribution to the central density. For $N = 258$ neutrons the situation lies somehow in between of the two previous cases due to the contribution of the 4p and 3f orbitals near the Fermi level. For the tin isotopes shown in Figure 13, the neutron orbits in the vicinity of the Fermi energy consist of a bunch of low angular momentum levels together with the intruder level of higher angular momentum. The neutron density profiles of the three tin isotopes show the normal pattern, though for $N = 50$ one can recognize a dip around the center which has the same nature discussed for the superheavy nucleus $N = 172$, now because of the 1g neutron level.

The proton density profiles of the three superheavy isotopes of $Z = 120$ depicted in Figure 13 show a similar pattern. Again, there is an effect due to the orbitals around the Fermi level. The 2f and 1i proton orbits of the $Z = 120$ nuclides push their protons away from the center and as a consequence the proton density develops a pocket around $r \sim 2$ fm. On the other hand, the increase of the proton density which is observed close to the origin is

reminiscent of the fingerprint of the 3s protons. The proton densities of the tin isotopes also exhibit a depression near the center. This time it is occasioned by the 1g proton level, which is the last filled level for $Z = 50$. However, due to the smaller Coulomb repulsion and to the 2p orbits close in energy to the 1g level, the effect is not as remarkable as for the proton density of $Z = 120$.

We now come to the discussion of the spin-orbit potential in the superheavy mass region, because it is responsible for the strong reduction of the spin-orbit splitting of low angular momentum energy levels found in the self-consistent calculations of SHE. In the relativistic models the spin-orbit force is automatically included in the interaction from the outset. It appears explicitly when the lower spinor of the relativistic wave function is eliminated in favor of the upper spinor. One then obtains a Schrödinger-like equation that contains a spin-orbit term which reads [24, 67]:

$$H_{so} = \frac{1}{2M^2} V_{so}(r) \mathbf{L} \cdot \mathbf{S}, \quad (10)$$

$$V_{so}(r) = \frac{M^2}{M^2} \frac{1}{r} \left(\frac{d\Phi}{dr} + \frac{dW}{dr} \right) + 2f_v \frac{M}{M} \frac{1}{r} \frac{dW}{dr}, \quad (11)$$

where we have made $\bar{M} = M - \frac{1}{2}(\Phi + W)$. This spin-orbit potential includes the contribution of the tensor coupling of the ω meson to the nucleon, which has an important bearing on the spin-orbit force [7, 12, 24]. For simplicity, we have neglected in (11) the small contributions of the ρ meson and of the Coulomb field which make $V_{so}(r)$ slightly different for neutrons and protons.

Figure 14 displays the radial dependence of V_{so} given by Eq. (11) for the isotopes of $Z = 120$ and $Z = 50$, whose density distributions we have just discussed. A common feature of both the tin and the superheavy isotopes is that, as expected, the spin-orbit potential develops a well at the surface region of the nuclear density distributions. As the system becomes more and more neutron rich, the depth of this well experiments a gradual reduction and the position of the bottom of the potential is shifted outwards, which brings about a weaker spin-orbit force.

There are two distinctive trends of the spin-orbit potential of superheavy nuclei with respect to normal nuclei. One is that the spin-orbit well at the

surface is less deep in the case of the SHE. The other one is the strong upward bump that V_{so} develops around 2 – 4 fm from the origin. This bump can be explained in connection with the spatial distribution of the densities. Consider the case of $N = 172$. The nucleon densities are sharply reduced in the center (Figure 13). To the extent that the meson fields follow the change of the densities, this causes V_{so} to develop a sharp bump in the interior of the nucleus [60, 63]. As seen from Figure 14, the ensuing bump is largest for $N = 172$ and decreases with increasing neutron number as the central region of the neutron densities flattens out.

The strong increase of V_{so} near the origin has an outstanding effect on the energy splitting of spin-orbit partner levels in SHE. Large angular momentum states whose wave function is mostly localized around the nuclear surface basically feel the attractive part of V_{so} , and thus present normal spin-orbit splittings. However, for low angular momentum states there is a strong overlap of the wave function with the positive region of V_{so} which dramatically reduces the spin-orbit splittings (they may even have the opposite sign for some parameter sets [60]). This effect is corroborated by looking at the splittings of spin-orbit partners in the SHE spectra represented in Figure 9.

Little differences are seen in Figure 14 between the predictions of the G2 and NL3 sets for the spin-orbit potential. The higher effective mass at saturation of G2 ($M_{\infty}^* = 0.66$) with respect to NL3 ($M_{\infty}^* = 0.6$) is compensated by the contribution of the tensor coupling f_v in the G2 set, since there exists a trade-off between the size of the ω tensor coupling and the size of the scalar field [12, 24]. As noticed in Ref. [19] the contribution of f_v to Eq. (11) accounts for roughly one-third of the spin-orbit strength in the case of the G2 parameter set.

Still, inspecting Figure 14, one may observe that the bottom of V_{so} is located at slightly larger values of r in the G2 set than in the NL3 set. Also, the spin-orbit well at the surface tends to be slightly deeper in G2 than in NL3 for the $Z = 120$ isotopes (the opposite happens for tin between $N = 50$ and $N = 82$). Finally, the upward bumps appearing in the spin-orbit potential of the SHE at $r \sim 3$ fm are larger if V_{so} is calculated with NL3. Thus, it may be expected

that the spin-orbit splitting of low angular momentum energy levels of SHE will be smaller with NL3 than with G2. Since for the SHE the strength of V_{so} at the surface is a little stronger and shifted towards slightly larger distances, the spin-orbit splitting for high angular momentum energy levels should be larger with G2 than with NL3. These predictions for the splittings of the energy levels of SHE coming from the small differences in V_{so} obtained with the two considered parameter sets, can be seen in the neutron single-particle spectra previously displayed.

VI. CONCLUDING REMARKS

The effective field theory model derived from the chiral effective Lagrangian proposed by Furnstahl, Serot and Tang [6] contains, in addition to the standard nonlinear RMF theory, other nonlinear scalar-vector, vector-vector and tensor couplings consistent with the underlying symmetries of QCD. The Lagrangian is expanded in powers of the fields and their derivatives and is organized in such a way that the results are not dominated by the highest-order terms retained. None of the couplings present in the expansion at a given order can be eliminated without a symmetry argument. The coupling constants and some meson masses of the truncated effective Lagrangian, or equivalently of the energy density functional, are taken as the effective parameters of the theory and are fitted to measured observables of a few doubly-magic nuclei (sets G1 and G2). Thus, the model can be interpreted as a covariant formulation of density functional theory where the effective functional approximates the exact (unknown) energy functional of the many-body nuclear system by expanding it in powers of auxiliary meson fields.

We have checked the extrapolations of the model to the infinite medium by comparing its results with the Dirac-Brueckner-Hartree-Fock calculations of nuclear and neutron matter above the normal saturation density. The sets G1 and G2 derived from the effective field theory predict a rather soft equation of state both around saturation and at high densities. These trends are in agreement with the output of the DBHF theory and recent experimental

observations from energetic heavy ion collisions [17, 18]. At variance with this, the standard nonlinear RMF parameter sets produce an EOS which is much too stiff with increasing density because of the restricted density dependence of the meson fields in the model.

We have analyzed the predictive power of the E-RMF model for describing finite nuclei in extreme conditions, like those found at the border of the nuclear chart. The study of exotic nuclei requires to include the pairing correlations. Our approach consisted of a modified BCS approximation with constant pairing matrix elements where the continuum is represented through the quasi-bound levels retained by their centrifugal barrier. It simulates the effects of the coupling to the continuum which are incorporated in more sophisticated treatments of the pairing correlation, like the relativistic Hartree-Bogoliubov approach or the resonant continuum-coupling BCS calculations that take into account the width of the resonant states [35, 37].

We studied very neutron-rich Zr isotopes up to the neutron drip line. Previous RHB calculations with the NL-SH set predict that these nuclei exhibit a giant halo [33]. This effect consists of a noticeable enhancement of the rms radius of the neutron density distribution due to the progressive occupancy of tiny bound levels above the $1h_{11/2}$ level which closes the shell with $N = 82$ neutrons. Our E-RMF calculations with the G2 parameter set produce comparable results to those obtained with RHB calculations with the NL-SH set. It is known that for stable medium and heavy nuclei the excitation energy of the isoscalar giant monopole resonance follows an $A^{-1/3}$ law. Non-relativistic calculations of the breathing mode in some neutron-rich nuclei showed that the RPA strength becomes broader as compared with normal isotopes and that a large amount of strength concentrates in the low-energy region, because of the transitions from weakly bound levels to the continuum. We have performed constrained Hartree calculations with G2 for the Zr chain. The results predict that the finite nuclei incompressibilities and the average excitation energy of the breathing mode should fall down steeply for the isotopes with the largest isospin content. This fact would reflect an enhancement of the low-energy part of the RPA strength when the nuclei approach the neutron drip line.

Moving to another edge of the nuclear landscape, we paid attention to the predictions of the E-RMF sets for the next spherical magic numbers beyond $Z = 82$ and $N = 126$. The determination of the shell closures in superheavy elements is more involved than in normal nuclei where a large gap in the level spectra usually signals the possible magic numbers, and one has to study other indicators like two-nucleon separation energies, two-nucleon shell gaps, and the pairing gap. We also analyzed the shell correction energy, which provides a stabilizing effect to superheavy nuclei against fission. Our spherical prospect must be understood in connection with the occurrence of double shell closures. Additional deformed shell closures may appear in the analyzed region of superheavy elements. We contrasted the density distributions and spin-orbit potentials of superheavy nuclei against those of normal mass nuclei, with some selected examples from near the proton drip line to near the neutron drip line. The G2 parameter set predicts strong shell closures for $Z = 120$ in combination with $N = 172$ and $N = 258$. Again, the E-RMF predictions for finite systems are in agreement with the results obtained with the fine tuned standard RMF parameter sets. Interestingly enough, the G2 set presents some indications of a shell closure for $Z = 114$ and $N = 184$, which the macroscopic-microscopic models have traditionally predicted to be a doubly magic nucleus.

In concluding we remark that we tried to show that in the quest for a unified mean field description of finite nuclei, even in exotic regions of the nuclear landscape, as well as of nuclear and neutron matter up to densities several times above the saturation density, the relativistic mean field model motivated by effective field theory is one reliable candidate. Surely, this is not the only way of obtaining such a unified description. Other implementations of effective field theory for the nuclear many-body problem, formulations of the relativistic model with inclusion of other mesons, or with density-dependent coupling vertices, may probably deliver also a consistent description similarly to the E-RMF model. Nevertheless, with the present findings we hope to have illustrated the plausibility and promising potential of the application of effective field theory methods to the nuclear structure problem.

Acknowledgments

T. S., M. C., and X. V. acknowledge financial support from the DGI (Ministerio de Ciencia y Tecnología, Spain) and FEDER under grant BFM2002-01868 and from DGR (Catalonia) under grant 2001SGR-00064. T. S. also thanks the Spanish Education Ministry grant SB2000-0411.

-
- [1] B. D. Serot and J. D. Walecka, *Adv. Nucl. Phys.* **16**, 1 (1986).
 - [2] P. Ring, *Prog. Part. Nucl. Phys.* **37**, 193 (1996).
 - [3] B. D. Serot and J. D. Walecka, *Int. J. Mod. Phys.* **E6**, 515 (1997).
 - [4] J. D. Walecka, *Ann. Phys. (N.Y.)* **83**, 491 (1974).
 - [5] J. Boguta and A. R. Bodmer, *Nucl. Phys.* **A292**, 413 (1977).
 - [6] R. J. Furnstahl, B. D. Serot, and H. B. Tang, *Nucl. Phys.* **A598**, 539 (1996).
 - [7] R. J. Furnstahl, B. D. Serot, and H. B. Tang, *Nucl. Phys.* **A615**, 441 (1997);
ibid **A640**, 505 (1998).
 - [8] H. Georgi, *Phys. Lett.* **B298**, 187 (1993).
 - [9] W. Kohn and L. J. Sham, *Phys. Rev. A* **140**, 1133 (1965).
 - [10] R. J. Furnstahl and B. D. Serot, *Nucl. Phys.* **A671**, 447 (2000).
 - [11] J. J. Rusnak and R. J. Furnstahl, *Nucl. Phys.* **A627**, 495 (1997).
 - [12] M. Del Estal, M. Centelles, and X. Viñas, *Nucl. Phys.* **A650**, 443 (1999).
 - [13] M. Del Estal, M. Centelles, X. Viñas, and S. K. Patra, *Phys. Rev. C* **63**, 024314 (2001).
 - [14] M. Centelles, M. Del Estal, X. Viñas, and S. K. Patra, *The Nuclear Many-Body Problem 2001*, NATO Science Series II Vol. 53 (Kluwer, Dordrecht, 2002), p. 97.
 - [15] R. Brockmann and R. Machleidt, *Phys. Rev. C* **42**, 1965 (1990).
 - [16] G. Q. Li, R. Machleidt, and R. Brockmann, *Phys. Rev. C* **45**, 2782 (1992).
 - [17] C. Sturm *et al*, *Phys. Rev. Lett.* **86**, 39 (2001); C. Fuchs, A. Faessler, E. Zabrodin, and Yu-Ming Zheng, *Phys. Rev. Lett.* **86**, 1974 (2001).
 - [18] P. Danielewicz, R. Lacey, and W. G. Lynch, *Science* **298**, 1592 (2002).

- [19] M. Del Estal, M. Centelles, X. Viñas, and S. K. Patra, Phys. Rev. C **63**, 044321 (2001).
- [20] M. A. Huertas, Phys. Rev. C **66**, 024318 (2002).
- [21] Tapas Sil, S. K. Patra, B. K. Sharma, M. Centelles, and X. Viñas, nucl-th/0310010, Phys. Rev. C (2004) in print.
- [22] P. Wang, Phys. Rev. C **61**, 054904 (2000).
- [23] J. C. Caillon, P. Gabinski, and J. Labarsouque, Nucl. Phys. **A696**, 623 (2001).
- [24] R. J. Furnstahl, J. J. Rusnak and B. D. Serot, Nucl. Phys. **A632**, 607 (1998).
- [25] B. C. Clark, R. J. Furnstahl, L. K. Kerr, J. J. Rusnak and S. Hama, Phys. Lett. **B427**, 231 (1998).
- [26] G. A. Lalazissis, J. König, and P. Ring, Phys. Rev. C **55**, 540 (1997).
- [27] G. Baym, Phys. Rev. **117**, 886 (1960).
- [28] Y. Sugahara and H. Toki, Nucl. Phys. **A579**, 557 (1994).
- [29] S. Typel and H. H. Wolter, Nucl. Phys. **A656**, 331 (1999); S. Typel, T. v. Chossy, and H. H. Wolter, Phys. Rev. C **67**, 034002 (2003).
- [30] P. -G. Reinhard, M. Rufa, J. Maruhn, W. Greiner, and J. Friedrich, Z. Phys. **A323**, 13 (1986).
- [31] I. Tanihata *et al*, Phys. Rev. Lett. **55**, 2676 (1985).
- [32] I. Tanihata, J. Phys. **G22**, 157 (1996).
- [33] J. Meng and P. Ring, Phys. Rev. Lett. **80**, 460 (1998).
- [34] J. Meng, H. Toki, J. Y. Zeng, S. Q. Zhang and S.-G. Zhou, Phys. Rev. C **65**, 041302 (1990).
- [35] J. Dobaczewski, H. Flocard, and J. Treiner, Nucl. Phys. **A422**, 103 (1984); J. Dobaczewski, W. Nazarewicz, T. R. Werner, J.-F. Berger, R. C. Chin, and J. Dechargé, Phys. Rev. C **53**, 2809 (1996).
- [36] N. Sandulescu, Nguyen Van Giai, and R. J. Liotta, Phys. Rev. C **61**, 061301 (2000).
- [37] N. Sandulescu, L. S. Geng, H. Toki, and G. C. Hillhouse, Phys. Rev. C **68**, 054323 (2003).
- [38] H. Hamamoto, H. Sagawa, and X. Z. Zhang, Phys. Rev. C **53**, 765 (1996); Phys. Rev. C **55**, 2361 (1997); Phys. Rev. C **56**, 3121 (1997).

- [39] E. Chabanat, P. Bonche, P. Haensel, J. Meyer, and R. Schaeffer, Nucl. Phys. **A635**, 231 (1998).
- [40] T. Maruyama, and T. Suzuki, Phys. Lett. **B219**, 43 (1989).
- [41] M. V. Stoitsov, P. Ring, and M. M. Sharma, Phys. Rev. **C50**, 1445 (1994).
- [42] M. V. Stoitsov, M. L. Cescato, P. Ring, and M. M. Sharma, J. Phys. **G20**, L149 (1994).
- [43] S. K. Patra, X. Viñas, M. Centelles and M. Del Estal, Nucl. Phys. **A703**, 240 (2002).
- [44] D. Vretenar, G. A. Lalazissis, R. Behnsch, W. Pöschl, and P. Ring, Nucl. Phys. **A621**, 853 (1997).
- [45] J. Piekarewicz, Phys. Rev. **C64**, 024307 (2001).
- [46] D. H. Youngblood, H.C. Clark, Y.-W. Lui, Phys. Rev. Lett. **82**, 691 (1999).
- [47] J. P. Blaizot, Phys. Rep. **64**, 171 (1980).
- [48] B. K. Jennings and A. D. Jackson, Phys. Rep. **66**, 141 (1980).
- [49] S. K. Patra, X. Viñas, M. Centelles and M. Del Estal, Phys. Rev. **C65**, 044304 (2002).
- [50] I. Bombaci and U. Lombardo, Phys. Rev. **C44**, 1892 (1991).
- [51] O. Bohigas, A. M. Lane and J. Martorell, Phys. Rev. **51**, 267 (1979).
- [52] S. Hofmann, Rep. Prog. Phys. **61**, 639 (1998); Eur. Phys. J. **A15**, 195 (2002); S. Hofmann, and G. Münzenberg, Rev. Mod. Phys. **72**, 733 (2000).
- [53] Yu. Ts. Oganessian *et al*, Eur. Phys. J. **A5**, 63 (1999); Nature **400**, 242 (1999); Eur. Phys. J. **A15**, 201 (2002).
- [54] T. Bürvenich, K. Rutz, M. Bender, P.-G. Reinhard, J. A. Maruhn, and W. Greiner, Eur. Phys. J. **A3**, 139 (1998).
- [55] P. Möller, and J. R. Nix, Nucl. Phys. **A549**, 84 (1992); J. Phys. **G20**, 1681 (1994).
- [56] R. Smolańczuk, Phys. Rev. **C56**, 812 (1997).
- [57] Zhongzhou Ren, Fei Tai, and Ding-Han Chen, Phys. Rev. C **66**, 064306 (2002).
- [58] S. Goriely, M. Samyn, P. -H. Heenen, J. M. Pearson, and F. Tondeur, Phys. Rev. C **66**, 024326 (2002).
- [59] T. Bürvenich, M. Bender, J. A. Maruhn, and P. -G. Reinhard, Phys. Rev. C

- 69**, 014307 (2004).
- [60] M. Bender, K. Rutz, P. -G. Reinhard, J. A. Maruhn, and W. Greiner, Phys. Rev. C **60**, 034304 (1999).
 - [61] A. T. Kruppa, M. Bender, W. Nazarewicz, P. -G. Reinhard, T. Vertse, and S. Ówiok, Phys. Rev. C **61**, 034313 (2000).
 - [62] M. Bender, W. Nazarewicz, P. -G. Reinhard, Phys. Lett. **B515**, 42 (2001).
 - [63] P. -G. Reinhard, M. Bender, and J. A. Maruhn, Comm. Mod. Phys. **2**, A177 (2002).
 - [64] B. Nerlo-Pomorska, K. Pomorski, J. Bartel, and K. Dietrich, Phys. Rev. **C66**, 051302 (2002).
 - [65] P. Ring and P. Schuck, *The Nuclear Many-Body Problem* (Springer-Verlag, Berlin, 1980).
 - [66] J. Meng and I. Tanihata, Nucl. Phys. **A650**, 176 (1999).
 - [67] G.A. Lalazissis, D. Vretenar and P. Ring, Phys. Rev. **C57**, 2294 (1998).

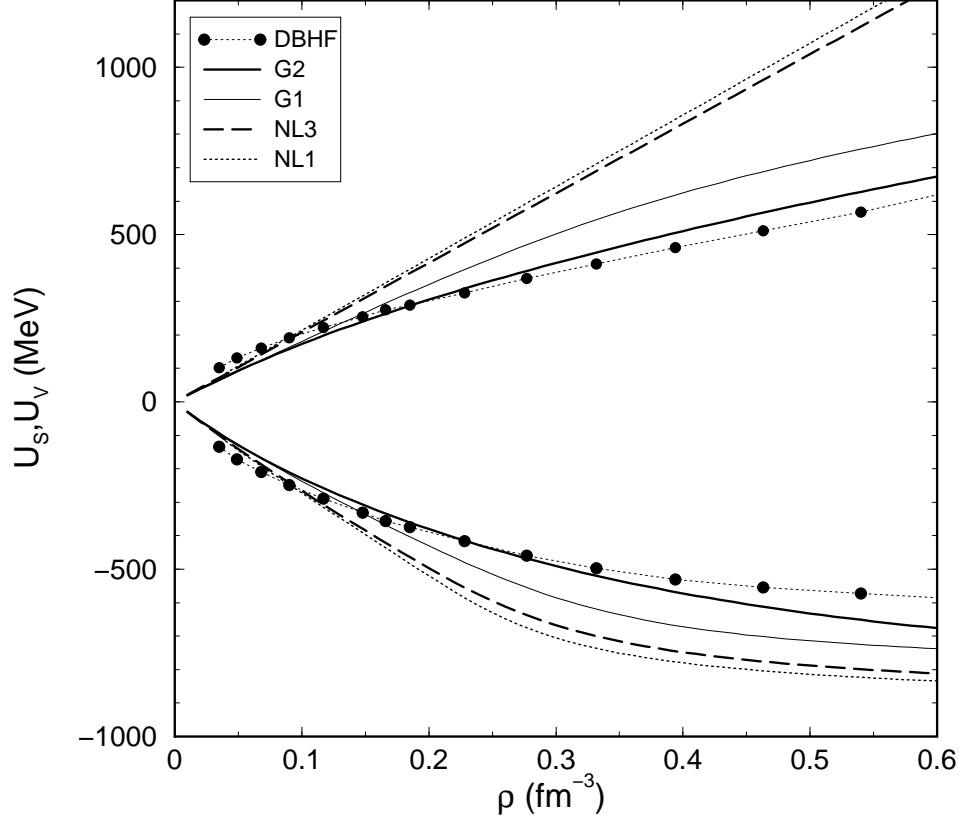


FIG. 1: The density dependence of the scalar (U_s) and vector (U_v) self-energies using the relativistic parameter sets NL1, NL3, G1, and G2 is compared with the result of the DBHF theory [15].

TABLE I: Parameters of the relativistic interactions used in this work, in dimensionless form, and their saturation properties in nuclear matter (energy per particle, density, incompressibility, effective mass, and symmetry energy coefficient).

	G1	G2	NL3
m_s/M	0.540	0.554	0.541
$g_s/4\pi$	0.785	0.835	0.813
$g_v/4\pi$	0.965	1.016	1.024
$g_\rho/4\pi$	0.698	0.755	0.712
κ_3	2.207	3.247	1.465
κ_4	-10.090	0.632	-5.668
ζ_0	3.525	2.642	0.0
η_1	0.071	0.650	0.0
η_2	-0.962	0.110	0.0
η_ρ	-0.272	0.390	0.0
α_1	1.855	1.723	0.0
α_2	1.788	-1.580	0.0
$f_v/4$	0.108	0.173	0.0
$f_\rho/4$	1.039	0.962	0.0
β_s	0.028	-0.093	0.0
β_v	-0.250	-0.460	0.0
a_v (MeV)	-16.14	-16.07	-16.24
ρ_∞ (fm ⁻³)	0.153	0.153	0.148
K (MeV)	215.0	215.0	271.5
M_∞^*/M	0.634	0.664	0.595
J (MeV)	38.5	36.4	37.40

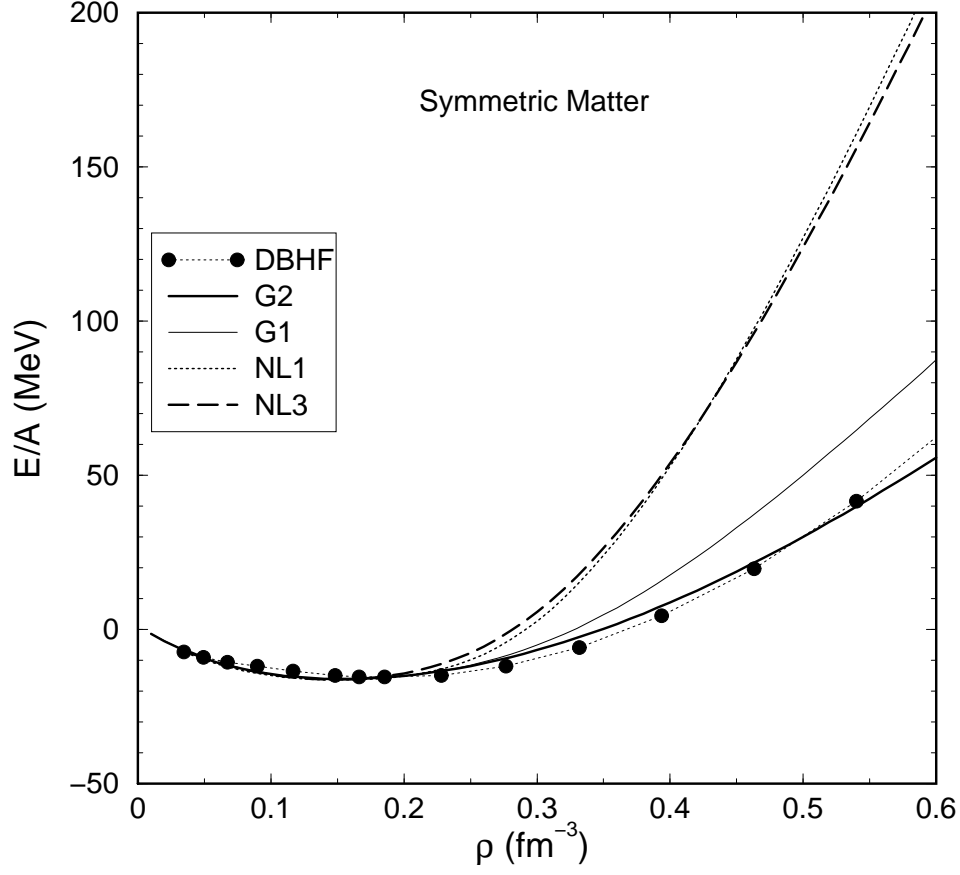


FIG. 2: Energy per particle of symmetric nuclear matter for the same cases as in Figure 1.

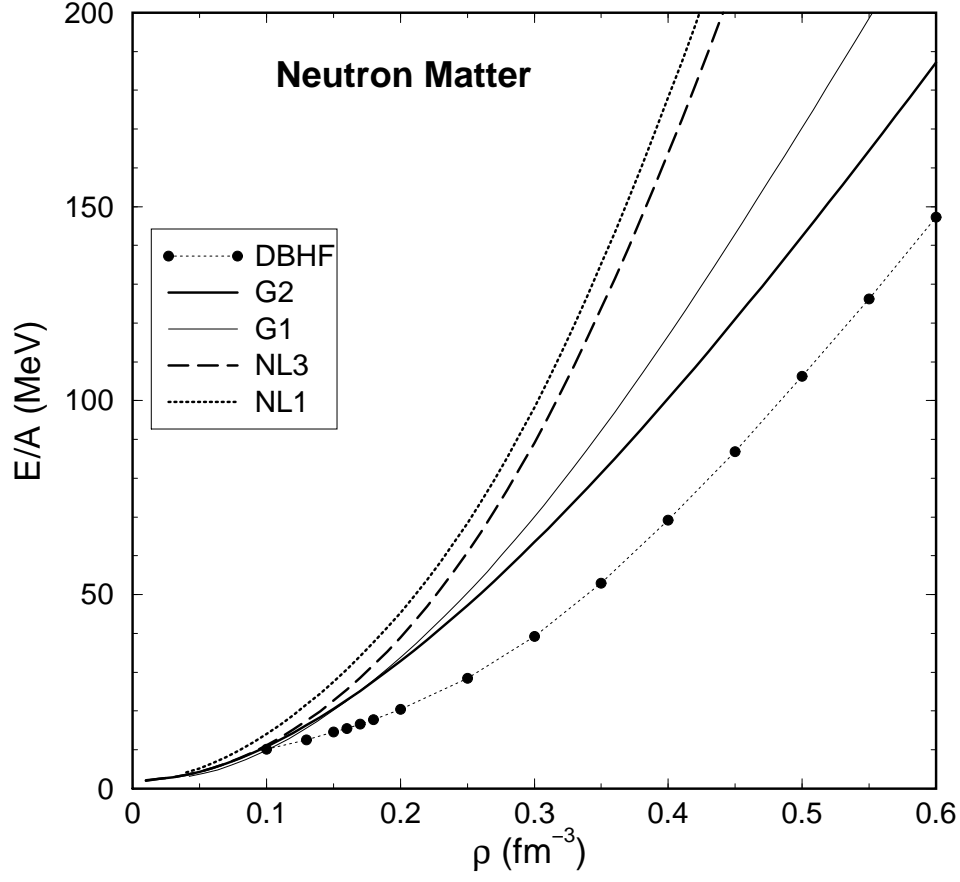


FIG. 3: Energy per particle of neutron matter for the same cases as in Figure 1.

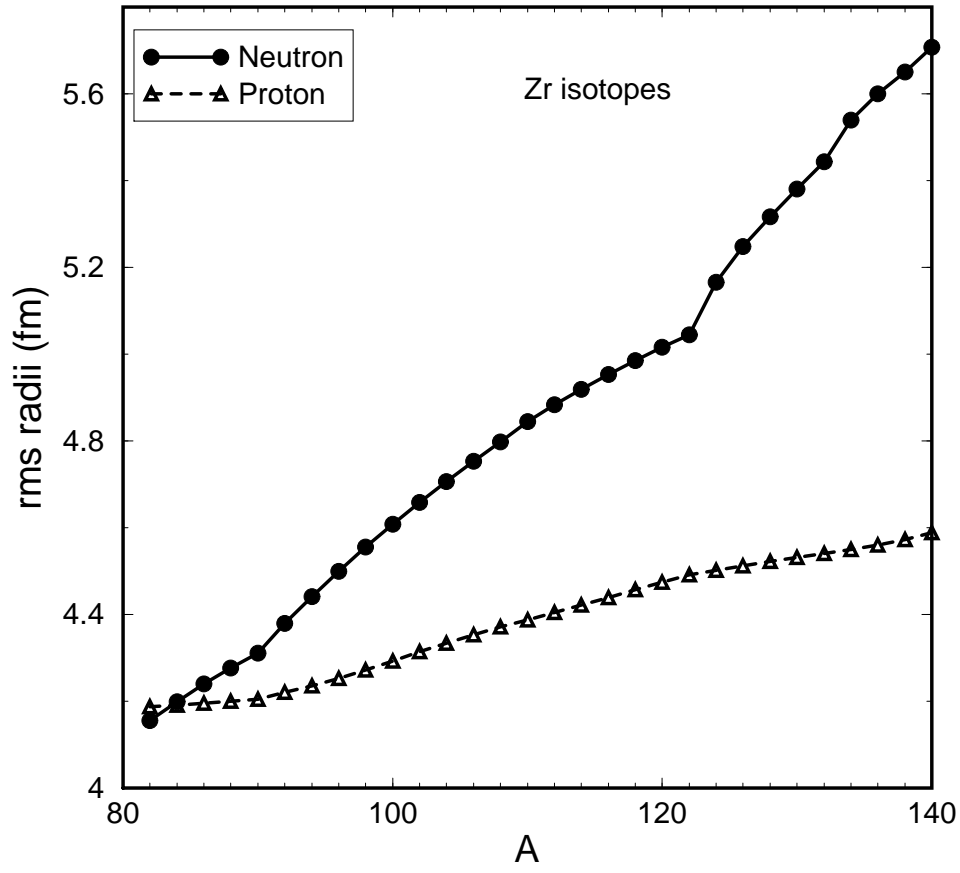


FIG. 4: Neutron and proton rms radii calculated with the G2 set for the Zr isotopic chain as a function of the mass number.

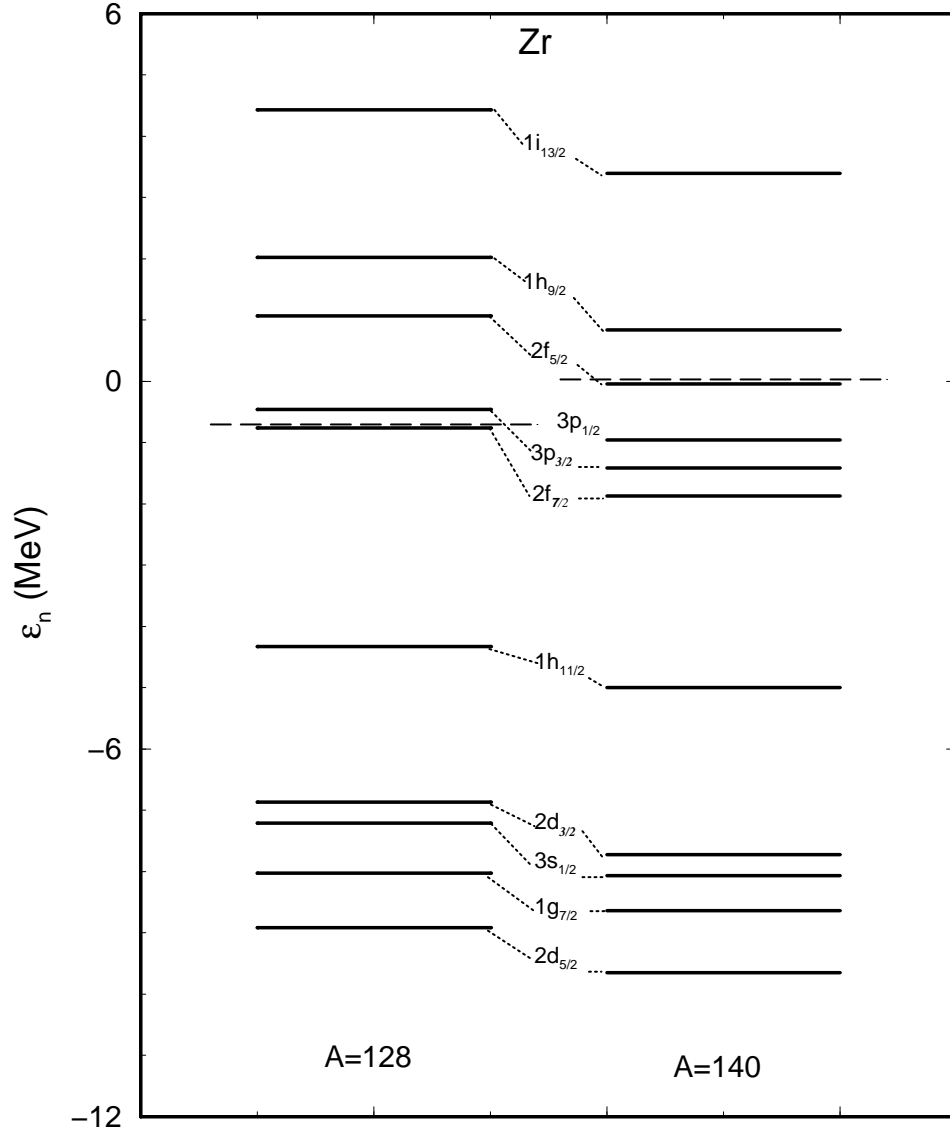


FIG. 5: Neutron spectra of the ^{128}Zr and ^{140}Zr isotopes as predicted by the G2 set.

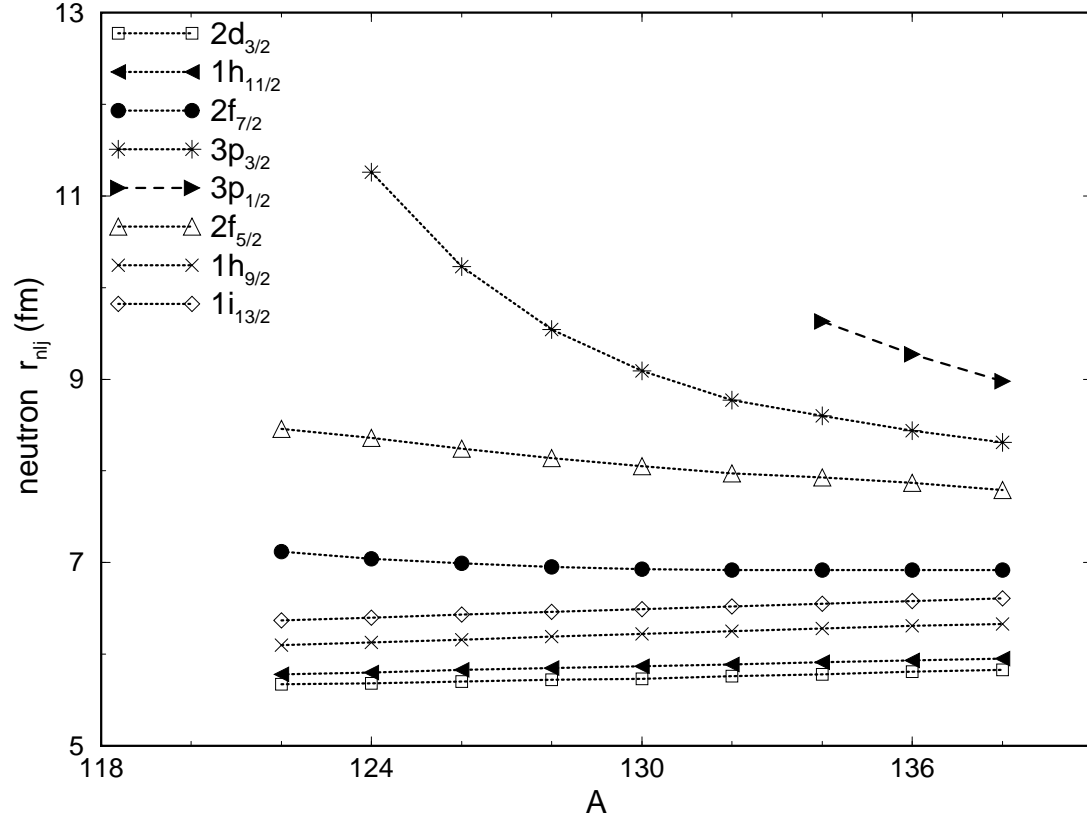


FIG. 6: Change with mass number of the rms radii of various neutron orbits for Zr isotopes calculated with the G2 force parameters.

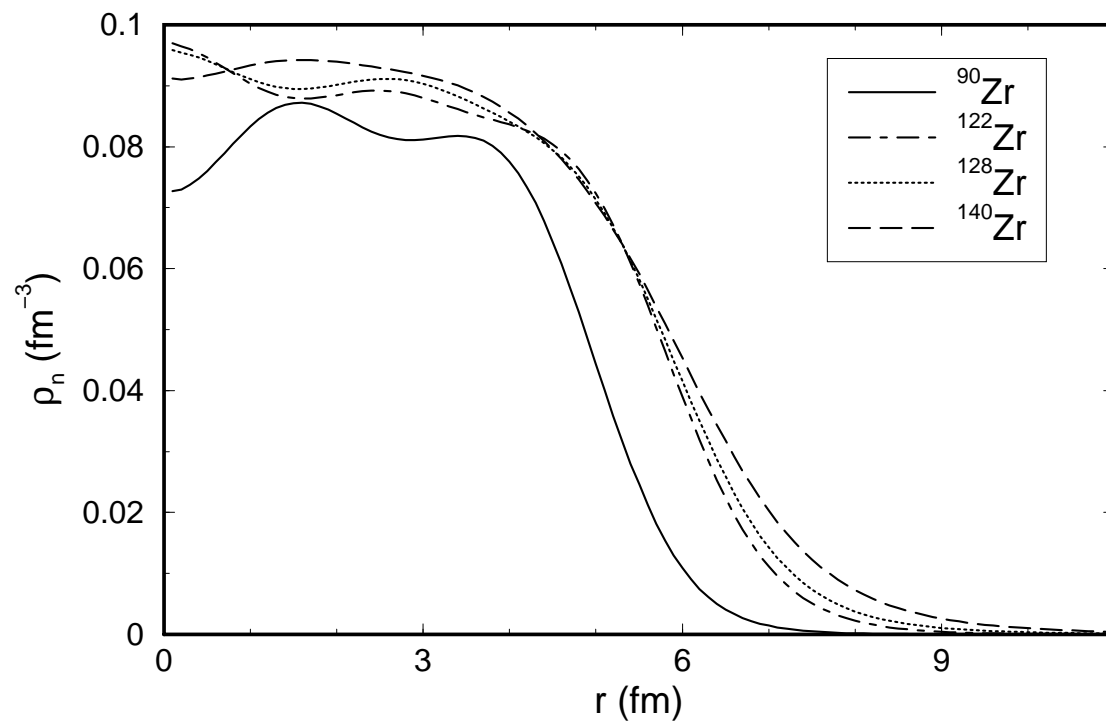


FIG. 7: Radial dependence of the neutron densities of Zr isotopes.

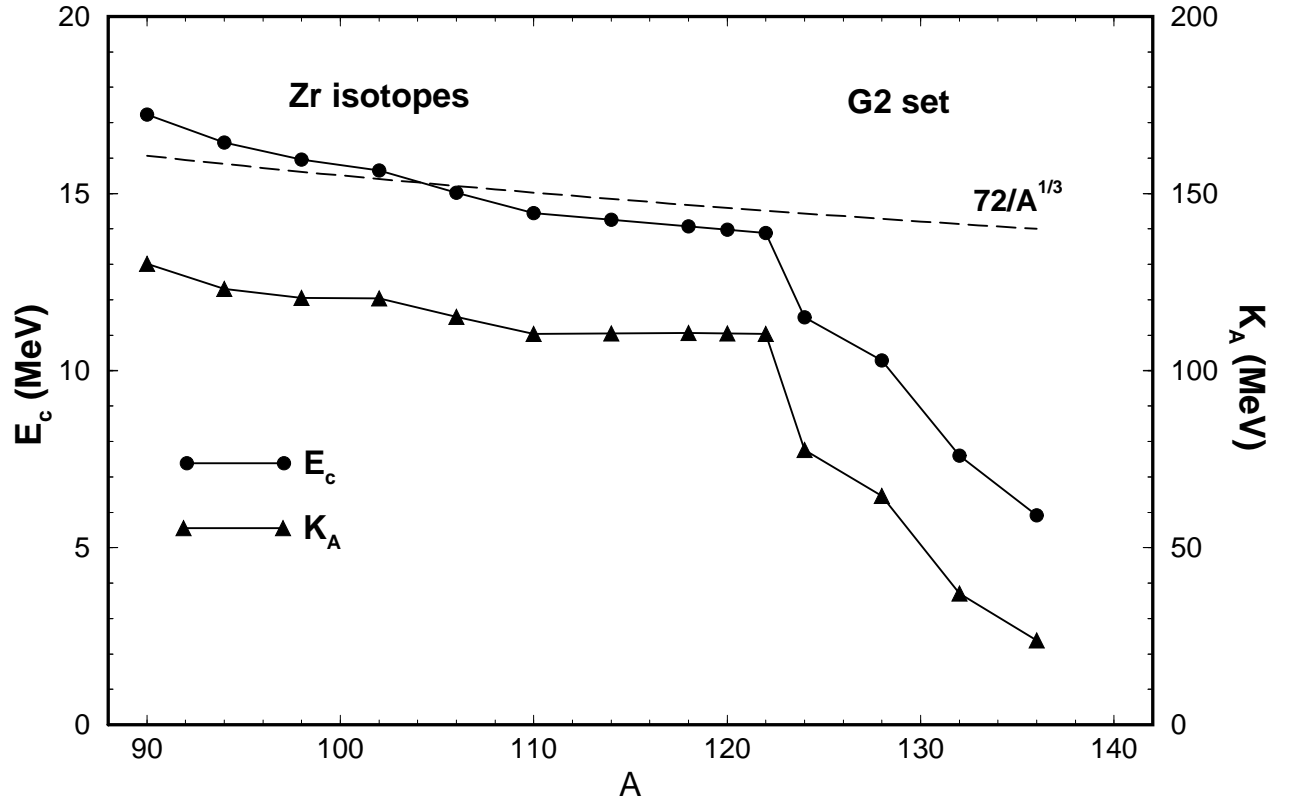


FIG. 8: Average energy E_c of the isoscalar giant monopole resonance and finite nucleus incompressibility K_A obtained from constrained calculations with the G2 set for Zr isotopes.

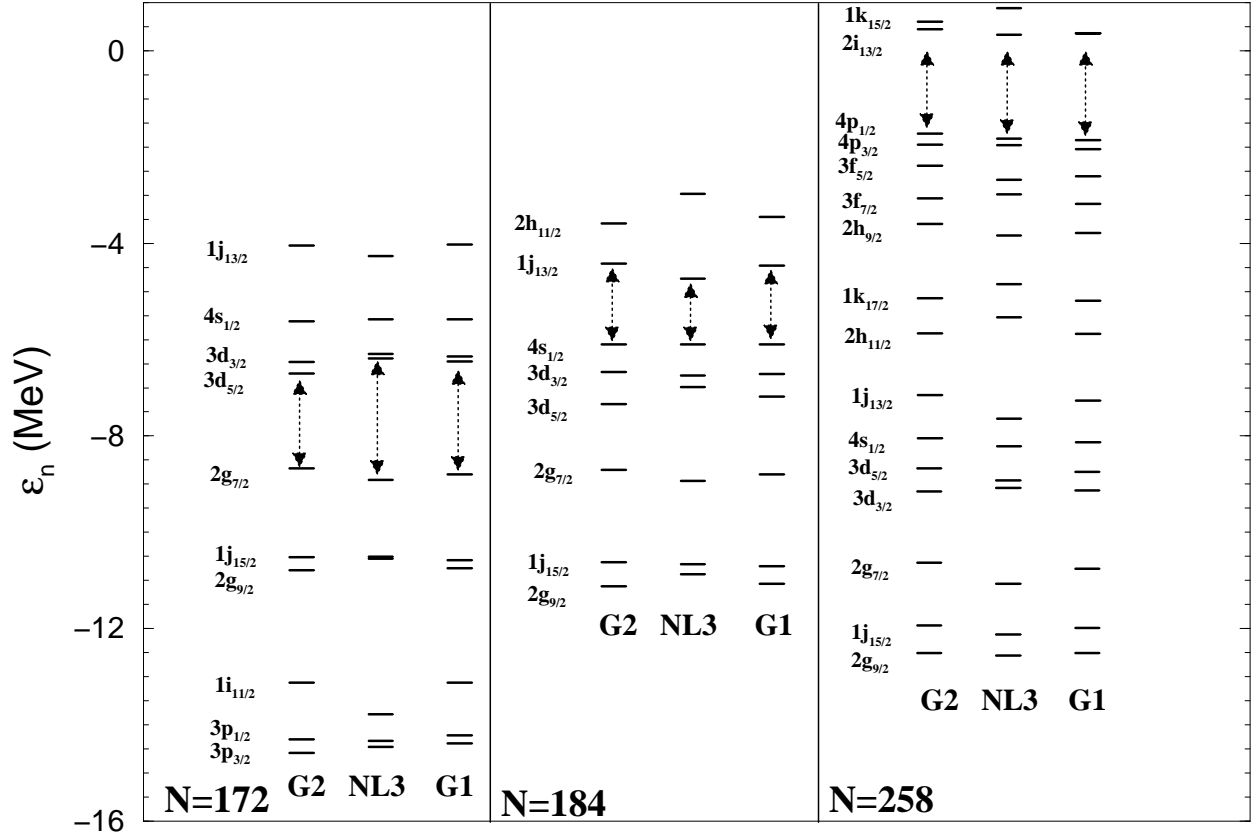


FIG. 9: Single-particle neutron spectra in the vicinity of the Fermi level for the superheavy isotopes $^{292}120$, $^{304}120$, and $^{378}120$ computed with the G1, G2 and NL3 parameter sets.

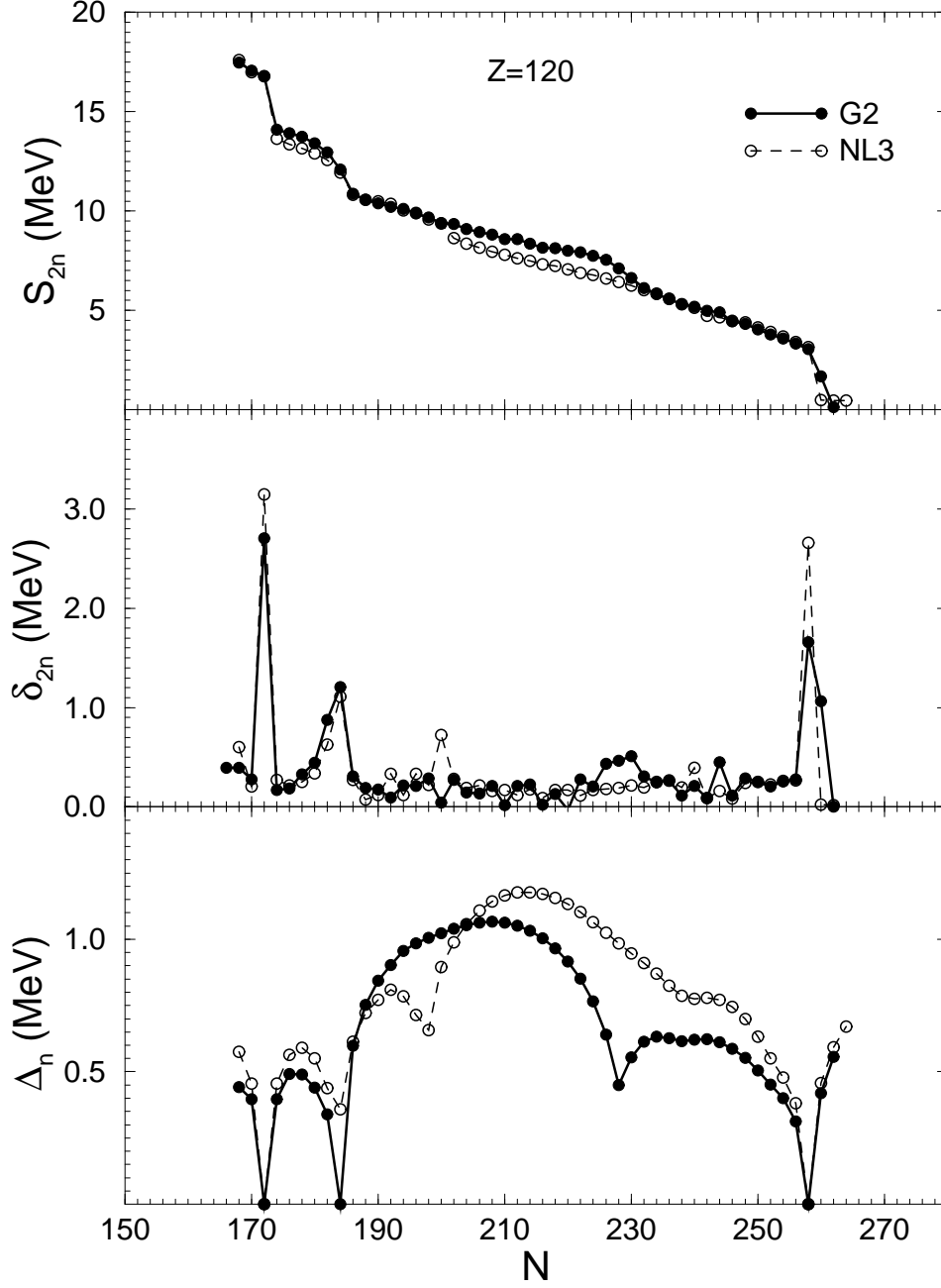


FIG. 10: Two-neutron separation energy S_{2n} , two-neutron shell gap δ_{2n} , and neutron average pairing gap Δ_n for $Z = 120$ isotopes obtained from spherical calculations with the relativistic parameter sets G2 and NL3. The proton average pairing gap Δ_p vanishes in the whole isotopic chain.

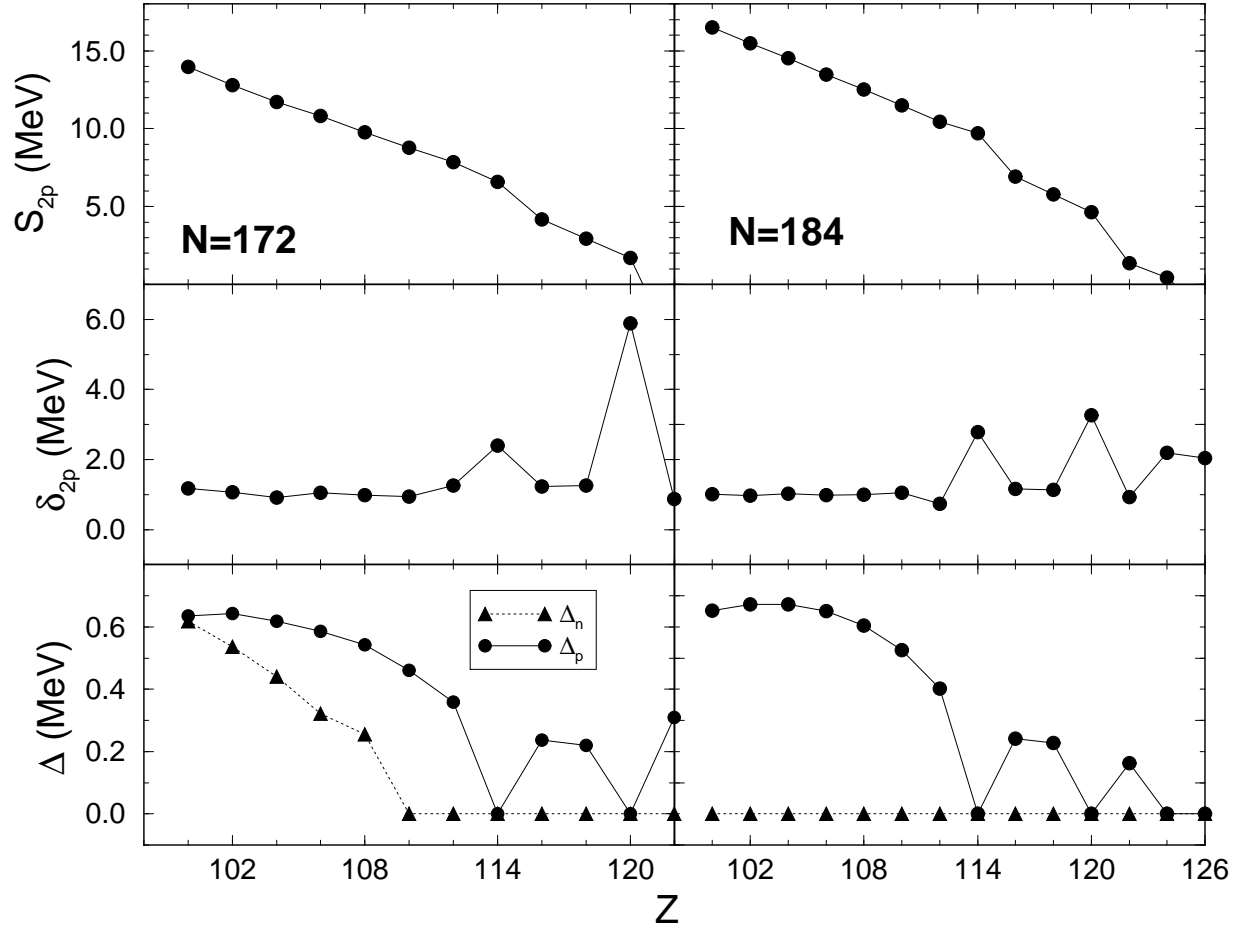


FIG. 11: Two-proton separation energy S_{2p} , two-proton shell gap δ_{2p} , and proton Δ_p and neutron Δ_n average pairing gaps for $N = 172$ and $N = 184$ isotones obtained from spherical calculations with the parameter set G2.

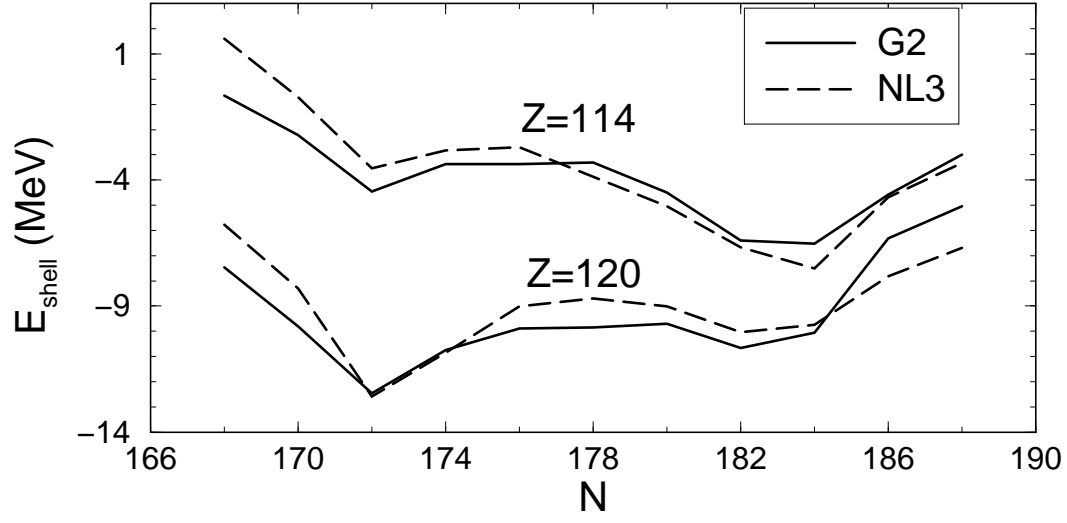


FIG. 12: Total shell correction energy for $Z = 114$ and $Z = 120$ isotopes in spherical calculations with the G2 and NL3 sets.

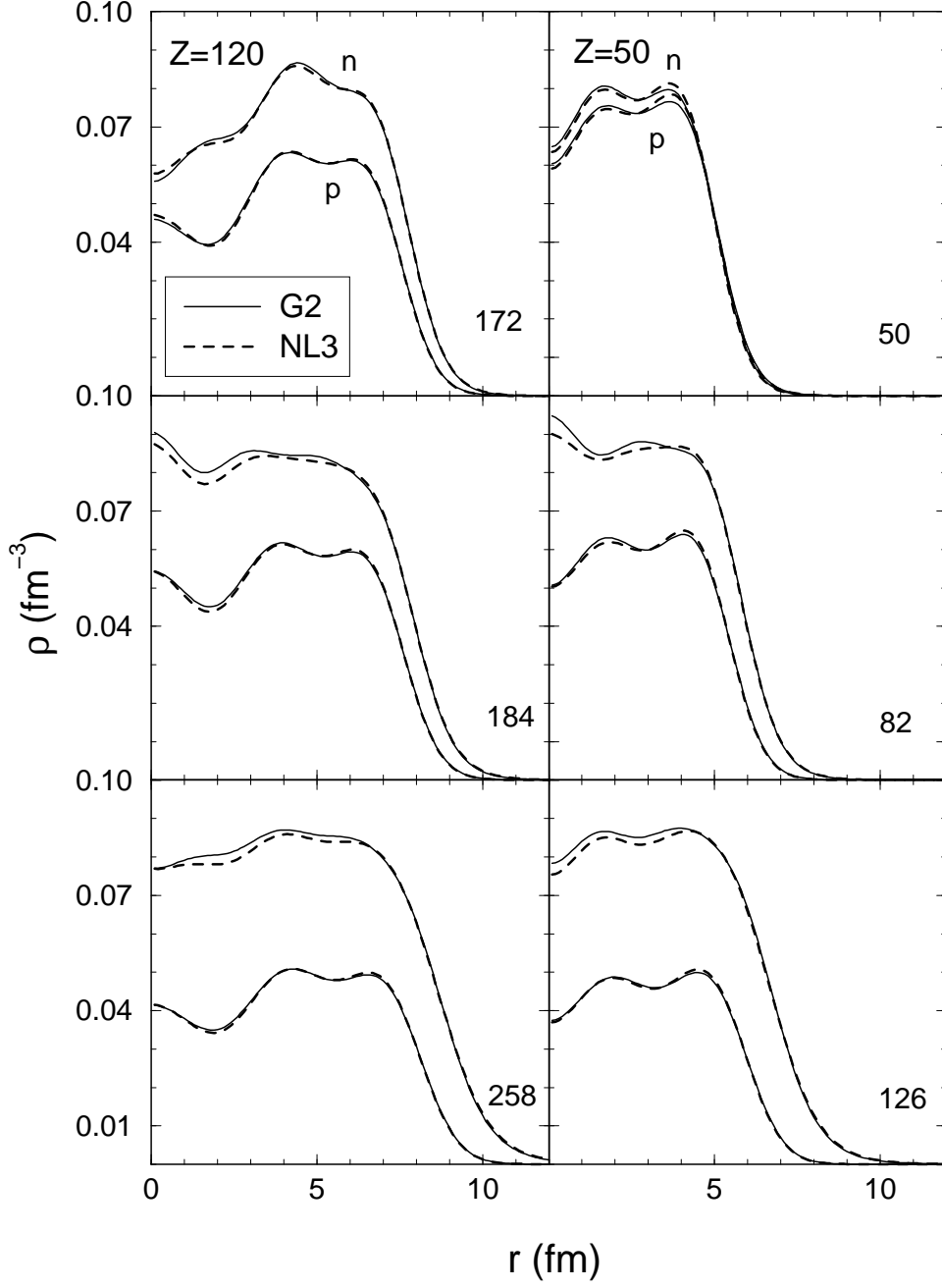


FIG. 13: The radial neutron and proton density distributions predicted by the sets G2 and NL3 for the $Z = 120$ superheavy isotopes with $N = 172$, 184 , and 258 (left panels), in comparison with the results for the tin isotopes with $N = 50$, 82 , and 126 (right panels).

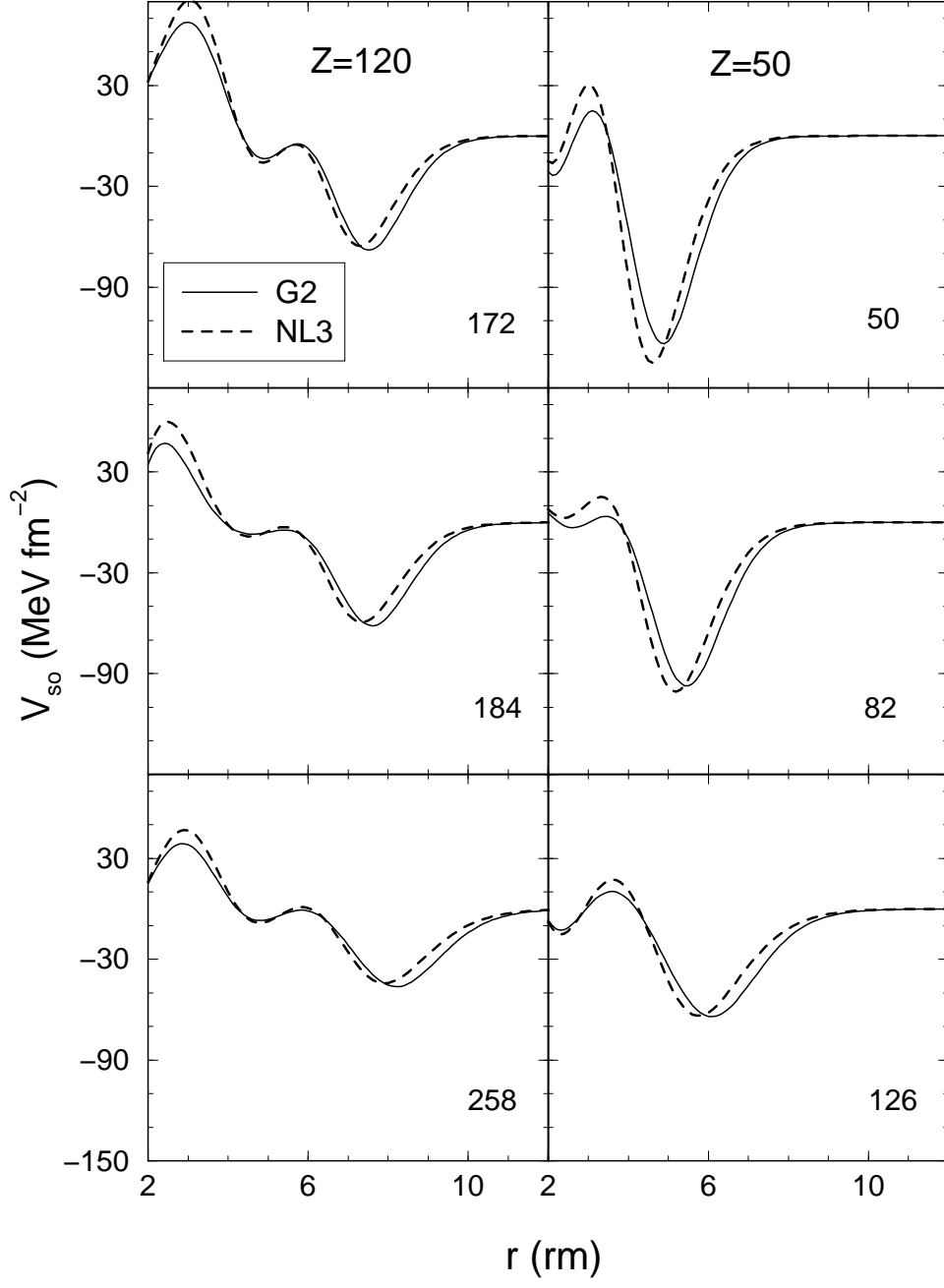


FIG. 14: Same as Figure 13 but for the radial dependence of the spin-orbit potential V_{so} defined in Eq. (11).